

**Advantage for tissue discrimination in anterior
and posterior eye by Multifunctional Jones
matrix OCT**

Arata Miyazawa

Submitted to the Graduate School of Pure and Applied
Sciences in Partial Fulfillment of the Requirements for the
Degree of Doctor of Philosophy in
Science Engineering

at the
University of Tsukuba

Abstract

I developed a tissue discrimination algorithm of polarization sensitive optical coherence tomography (PS-OCT) based on the optical properties of tissues. I calculated the three-dimensional (3D) feature vector from the parameters intensity, extinction coefficient, birefringence, which were obtained by PS-OCT. The tissue type of each pixel was determined according to the position of the feature vector in the 3D feature space. The algorithm was applied for discriminating tissues of the human anterior eye segment. The conjunctiva, sclera, trabecular meshwork (TM), cornea, and uvea were well separated in the 3D feature space, and we could observe them with good contrast. The TM line can be observed in the 3D discriminated volume, as observed by gonioscopy. I validated this method by applying this algorithm and histological data to porcine eyes. A marker was injected into sub-Tenons space and the tissues that were anterior to the marker and posterior to the marker were successfully segmented by this algorithm.

Jones matrix-based polarization sensitive optical coherence tomography (JM-OCT) simultaneously measures optical intensity, birefringence, degree of polarization uniformity, and OCT angiography. The statistics of the optical features in a local region, such as the local mean of the OCT intensity, are frequently used for image processing and the quantitative analysis of JM-OCT. Conventionally, local statistics have been computed with fixed-size rectangular kernels. However, this results in a trade-off between image sharpness and statistical accuracy. I introduce a superpixel method to JM-OCT for generating the flexible kernels of local statistics. A superpixel is a cluster of image pixels that is formed by the pixels' spatial and signal value proximities. An algorithm for superpixel generation specialized for JM-OCT and its optimization methods are presented. The spatial proximity is in two-dimensional cross-sectional space and the signal values are the four optical features. Hence, the superpixel method is a six-dimensional clustering technique for JM-OCT pixels. The performance of the JM-OCT superpixels and its optimization methods are evaluated in detail using JM-OCT datasets of posterior eyes. The superpixels were found to well preserve tissue structures, such as layer structures, sclera, vessels, and retinal pigment epithelium. And hence, they are more suitable for local statistics kernels than conventional uniform rectangular kernels.

I also calculated birefringence with superpixel kernels and this improved discrimination ability of the NFL in posterior eye.

Multifunctional JM-OCT has a great advantage for tissue discrimination in anterior and posterior eye.

Acknowledgments

Special thanks are due to Professor Masahide Itoh, who was my supervisor before leave of absence and withdrawal due to illness. Without his support and guidance, my work would not have been continued. I would like to thank Professor Yoshiaki Yasuno and colleagues in Computational Optics Group for their invaluable support and guidance through the hard moments of this research. I am also grateful to my dissertation committee: Professor Masahiro Sasaki for their support to this thesis.

Contents

Abstract	i
Acknowledgments	iii
List of figures	vi
List of tables	vii
1 Introduction	1
2 Tissue discrimination in anterior eye	3
2.1 Tissue discrimination method in anterior eye	4
2.1.1 PS-OCT system	4
2.1.2 Features of the tissue being studied	5
2.1.3 Tissue discrimination	5
2.1.4 Display of the discrimination results	6
2.1.5 3D tissue discrimination	7
2.2 Results of tissue discrimination in anterior eye	7
2.3 Discussions	11
2.3.1 Comparison with histological analysis	11
2.3.2 Advantage of 3D feature spaces	12
2.3.3 Selection of the reference regions	14
2.3.4 Error in BR measurement	14
2.4 Conclusions	16
3 Improvement of tissue discrimination ability in posterior eye	17
3.1 JM-OCT system and measurement protocol	18
3.2 Generation and optimization of superpixels for JM-OCT	18
3.2.1 Superpixel generation	19
3.2.2 Optimization method of superpixel parameters	20
3.3 Validation of the superpixel in posterior eye	23
3.3.1 Validation of the superpixel parameter optimization methods	23
3.3.2 Superpixelization of <i>in vivo</i> posterior eye image	27
3.4 Birefringence estimation using superpixel kernel in posterior eye	30
3.5 Discussions	30
3.5.1 Optimal definition of spatial distance	30
3.5.2 Universality of the optimized weights of the optical features	30
3.5.3 Computational time	34
3.6 Conclusions	36

List of Figures

2.1	Feature distributions of the 5 reference regions in the 3D feature space . . .	8
2.2	Results of the tissue discrimination	9
2.3	Gonioscopic images obtained by 3D discriminated volume	10
2.4	Validation of the tissue discrimination result with in vitro porcine eye . .	11
2.5	Feature distributions in the 2D feature spaces	12
2.6	The normalized distances of all the pairs of the 5 reference regions in each feature space	13
2.7	An example of the selection of reference regions	15
3.1	Flow of optimization for parameters used in superpixel generation	24
3.2	The alteration of the weights of the optical features during iterative opti- mization	25
3.3	The alterations of the cost function and the contribution metrics of each optical feature during the iterative optimization of the weights	25
3.4	Superpixels generated with several compactness factor configurations . . .	26
3.5	Mean normalized-ISPVs for several compactness factor configurations . .	27
3.6	An example of the superpixelization of an ONH	28
3.7	An example of the superpixelization of a macula	29
3.8	Birefringence of the macula with rectangle kernel and superpixel kernel .	31

List of Tables

3.1	Validation for intra-dataset universality examined with an ONH	33
3.2	Validation for intra-dataset universality examined with a macula	33
3.3	Validation of inter-dataset-and-intra-subject universality with ONH datasets	34
3.4	Validation of inter-dataset-and-intra-subject universality with macular datasets	34
3.5	Validation of inter-subject universality with ONH datasets	35
3.6	Validation of inter-subject universality with macular datasets	35

Chapter 1

Introduction

Medical imaging technique has been greatly developed and had a significant impact for medical field in recent decade. Optical coherence tomography (OCT) have developed as a result of the improvement in the filed of fiber optics, light sources, optical components and detectors, and so on. OCT uses partially coherent near-infrared light and detects backscattered light from the sample with the help of a low-coherence interferometer. Because OCT has the potential to produce high-resolution images at near-video rates, it is expected to be used for the diagnosis of diseases especially in ophthalmology.

OCT has been developed to measure several optical properties. Polarization sensitive-OCT (PS-OCT) is an extension of conventional OCT, which can measure birefringence (phase retardation, optic axis, and diattenuation [1,2]) in addition to backscattering intensity. The birefringence measured by PS-OCT is considered to be caused by collagen fibrous tissue. The degree of polarization uniformity (DOPU) [3,4] can be also obtained by PS-OCT. Low DOPU signal is considered to be an indicator of melanin [5]. OCT angiography (OCTA) is another extension of OCT, which provides vascular information through the time variation analysis of OCT signals [6,7]. Jones matrix-based PS-OCT (JM-OCT) provides all of the above mentioned optical properties: scattering intensity, local birefringence (BR)/phase retardation, DOPU, and OCTA using a single scan [8,9]. This JM-OCT is called multifunctional JM-OCT.

Glaucoma is the second most common cause of blindness worldwide. Early detection of the glaucoma is important because the vision loss due to glaucoma can not be recovered. Optical coherence tomography (OCT) can provide cross-sectional image of the eye [10] and OCT is used for the diagnosis of glaucoma and other eye diseases.

OCT has been used to identify the tissue types of highly scattering biological structures. Segmentation of retinal layers is clinically important because quantitative measurement of their thickness may be used to diagnose diseases. For instance, the thickness of the retinal nerve fiber layer is related to glaucoma, and the thickness of the retinal pigment epithelium (RPE) is related to age related macular degeneration. In the field of ophthalmology, a levelset segmentation algorithm based on structural information was developed for the posterior eye and the retinal layers were segmented [11,12].

However, segmentation based on structural information of the anterior eye is difficult because the scattering properties of tissues in the anterior eye are not so different [13,14]. On the other hand, there is a clinical demand for the differentiation of the specific tissue type. For example, The TM is a drainage of the aqueous humor of the anterior eye chamber and controls intraocular pressure. If drainage from the TM is blocked, the pressure in the eye, i.e., the intraocular pressure, increases, resulting in angle-closure glaucoma. Hence, the position of the TM is demanded to differentiate from other tissues

in the anterior eye and it can be used as a landmark for screening patients for the risk of angle-closure glaucoma.

Therefore, I attempted to develop an algorithm for differentiating between tissues on the basis of their optical properties and not structural information by OCT. As I mentioned before, the multifunctional JM-OCT can provide four optical properties and suitable for that purpose.

Chapter 2 describes the algorithm for differentiating between tissues in anterior eye on the basis of their optical properties. The birefringence measured by PS-OCT is useful for tissue discrimination in the anterior eye because collagen fibrous tissue of the sclera and TM can be observed as the increase in phase retardation along the depth [15,16]. I tried to develop the tissue discrimination algorithm by using three dimensional feature space, which uses three optical features. This algorithm created a clinically useful image for angle assessment related to glaucoma.

In Chapter 3, I also tried to improve tissue discrimination ability of the multifunctional JM-OCT. The accuracy of the tissue discrimination algorithm can be improved by the increasing of the accuracy of optical properties. Birefringence values in each pixel are calculated in the local regions around the each pixel. These local regions are called as kernel. I developed the method to generate more suitable kernel for calculating birefringence. In this method, I used the four optical properties to cluster pixels in the identical tissue type and these clustered pixels were used as kernel. Birefringence was recalculated by using these kernels and more accurate birefringence values were obtained. This study was performed in posterior eye tentatively because there are clear vessels and melanin rich tissue and the performance can be evaluated properly than in the anterior eye.

Chapter 2

Tissue discrimination in anterior eye

Optical coherence tomography (OCT) can be used to obtain information on the cross-sectional structure of biological samples [10]. OCT uses partially coherent near-infrared light and detects backscattered light from the sample with the help of a low-coherence interferometer. Because OCT has the potential to produce high-resolution images at near-video rates, it is expected to be used for the diagnosis of diseases.

OCT has been used to identify the tissue types of highly scattering biological structures such as the skin [17], vascular tissue [18], gastrointestinal tract [19], urinary bladder [20], and prostate [21]. In these cases, identification is based on the structural information, e.g., the presence or absence of structures and layers as visualized by the scattering intensity.

On the other hand, many normal tissues, such as the sclera and aorta, show few structures in OCT images and classification of these tissues seems to be difficult. When visible structural features cannot be observed, texture analysis is useful for distinguishing between tissue types. Texture analysis was first used for classifying normal and abnormal mouse tissues [22]. Texture analysis has been applied for the diagnosis of dysplasia in the esophagus [23] and cancer in the urinary bladder [24]. Moreover, breast cancer has also been diagnosed by image analysis [25].

These reports suggest that the difference in the optical properties of tissue types are well acquired by OCT, even when no visible structure can be observed in the scattering OCT image.

In the field of ophthalmology, a levelset segmentation algorithm based on structural information was developed for the posterior eye, and the retinal layers were segmented [11,12,26,27]. Segmentation of retinal layers is clinically important because quantitative measurement of their thickness may be used to diagnose diseases. For instance, the thickness of the retinal nerve fiber layer is related to glaucoma, and the thickness of the retinal pigment epithelium (RPE) is related to age related macular degeneration.

However, segmentation based on structural information of the anterior eye is difficult because the scattering properties of tissues in the anterior eye are not so different [13, 28–31]. However, there is a clinical demand for the differentiation of the trabecular meshwork (TM) from other tissues in the anterior eye. The TM is a drainage of the aqueous humor of the anterior eye chamber and controls intraocular pressure. If drainage from the TM is blocked, the pressure in the eye, i.e., the intraocular pressure, increases, resulting in angle-closure glaucoma. Hence, the position of the TM can be used as a

landmark for screening patients for the risk of angle-closure glaucoma. Therefore, I attempted to develop an algorithm for differentiating between tissues in the anterior eye on the basis of their optical properties and not structural information.

There were some reports on tissue discrimination based on optical parameters obtained by OCT. Xu et al. characterized 3 types of atherosclerosis plaques in coronary arteries was performed by analysis of 2 optical parameters obtained by OCT [14]. The results of this report indicate that a combination of 2 parameters offers better discrimination; moreover, it is well known that analysis in a higher dimensional feature space can increase the accuracy of segmentation [32].

In the report of Mujat et al., differentiating of 3 breast tissue types was demonstrated by analysis of 8 parameters obtained by OCT [33]. This report also indicate that analysis in a higher dimensional space is expected to produce better classification.

Segmentation of the RPE was performed by Göttinger et al. by using optical parameters obtained by polarization sensitive-OCT (PS-OCT) [3]. PS-OCT is an extension of conventional OCT, which can measure birefringence (phase retardation, optic axis, and diattenuation [1, 2, 34–37]) in addition to backscattering intensity. RPE segmentation was performed by the broad distribution of retardation values caused by polarization scrambling at the RPE. I think that the birefringence measured by PS-OCT is also useful for tissue discrimination in the anterior eye. Because of the increase in phase retardation along the depth, which indicates birefringence [38, 39], collagen fibrous tissue of the sclera and TM can be observed in the phase-retardation image of the anterior eye [15, 16].

In this paper, I demonstrate an algorithm for discriminating between tissues in the anterior eye and create a clinically useful image for angle assessment related to glaucoma. With this aim, I used the results of the previous reports. That is, I calculated the optical parameters of tissues based on both intensity and birefringence as measured by PS-OCT and conducted the analysis by using a combination of 3 optical parameters.

2.1 Tissue discrimination method in anterior eye

I measured 4 eyes of 4 subjects by PS-OCT and applied the following discrimination algorithm. I calculated 3 optical property values that were measured by PS-OCT. These properties were used as features of the tissue being analyzed. Hence, each pixel has a set of 3 feature values, which are together referred to as the three-dimensional (3D) feature vector. If adequate features are used, the distributions of the feature vectors of different tissues will be separated in a corresponding 3D feature space. All pixels can be discriminated to identify the types of tissues according to the positions of the feature vectors in the feature space.

2.1.1 PS-OCT system

The OCT system employed in this study was polarization sensitive swept source OCT (PS-SS-OCT) with source polarization modulation [16]. This system can be used to calculate OCT intensity, diattenuation, phase retardation, and relative optic axis orientation of the sample on the basis of the measured Jones matrix. The center wavelength of the light source was $1.31 \mu\text{m}$, and the scanning rate was 20,000 A-lines/s. The axial and lateral resolutions were $11.9 \mu\text{m}$ and $32.3 \mu\text{m}$, respectively. The image size of the B-scan was 605 (axial) \times 512 (lateral) pixels, obtained from the measurement range of $4 \times 5 \text{ mm}$.

The examination protocol of PS-OCT was designed to adhere to the tenets of the Declaration of Helsinki and was approved by the institutional review boards of the University of Tsukuba.

2.1.2 Features of the tissue being studied

The parameters used in this study were backscattered intensity (I), extinction coefficient (EC), and birefringence (BR).

The backscattered intensity with a linear scale, which was calculated as the sum of the intensities of horizontally and vertically polarized zeroth-order OCT signals [16], was used as a feature of the tissues (I).

The extinction coefficient is calculated as the slope of the logarithmic intensity along the depth (EC). This slope can be considered as a sum of the scattering coefficient, absorption coefficient, and systematic OCT signal decay. Since the decay is the same for each A-scan, this coefficient is regarded as an optical property of tissues. The least squares fitting is applied to the logarithmic intensity to obtain the slope with a kernel size of 45 pixels (297 μm).

Although phase-retardation OCT images show the presence of birefringence as the increase of retardation along the depth, the raw phase retardation could not be used as a feature parameter. This is because retardation measured by PS-OCT is cumulative along the depth, which means that birefringence is not indicated by the value of retardation, but by the increase ratio of retardation along the depth. Additionally, the range of retardation is limited to 180 degrees because of phase wrapping. Therefore, I calculated local birefringence based on Jones matrix [40] with a kernel size of 14 pixels (93 μm) and used it as a feature of the tissues (BR).

For reducing the noise effect of speckle, the mean value of pixels in a moving window (size: 15 \times 15 pix = 99 μm (axial) \times 146 μm (lateral)) was calculated as the value of each feature (I, EC, and BR) and used for analysis.

2.1.3 Tissue discrimination

The region that can be considered to be a part of a target tissue is selected manually as a reference region. I set the following 5 target tissues and selected 5 reference regions for each: the conjunctiva, sclera, TM, cornea, and uvea. This selection was based on the anatomical and histological features of the tissues. The combination of 3 features, i.e., the 3D feature vector, was plotted in the 3D feature space. Then, from these plots, I created similarity distribution maps for each reference region. These similarity distribution maps were calculated as the sum of Gaussian kernels in order to ensure that the distributions in the feature space were smooth and continuous. Namely, the similarity distribution map of the i -th reference region is defined as

$$D_i(\mathbf{x}) \equiv \sum_{j=0}^{M_i-1} G(\mathbf{x} - \boldsymbol{\mu}_{i,j}), \quad (2.1)$$

where i is the ID of reference regions, i.e., the ID of tissue type, with a range of $[0, N-1]$; N , the number of reference regions; j , the pixel ID in the reference region, with a range of $[0, M_i-1]$; M_i , the number of pixels in the i -th reference region; $\mathbf{x} = [x_0 \cdots x_k \cdots x_{M-1}]$, coordinate in the M -dimensional feature space; k , ID of the features used for the discrimination, with a range of $[0, L-1]$; L , the number of features; $\boldsymbol{\mu}_{i,j} = [\mu_{i,j,0}, \cdots, \mu_{i,j,k}, \cdots, \mu_{i,j,L-1}]$, coordinate of the j -th pixel of the i -th reference

region in the feature space; $\mu_{i,j,k}$, value of the k -th feature of the j -th pixel in the i -th reference region. $G(\mathbf{x})$ is a Gaussian kernel in the feature space and is defined as

$$G(\mathbf{x}) = \exp \left[-\frac{1}{2} \sum_{k=0}^{L-1} \left(\frac{x_k}{\sigma_k} \right)^2 \right] = \exp \left[-\frac{1}{2} \frac{\mathbf{x} \cdot \mathbf{x}^T}{\boldsymbol{\sigma} \cdot \boldsymbol{\sigma}^T} \right], \quad (2.2)$$

where $\boldsymbol{\sigma}$ determines the kernel size, which is defined as

$$\boldsymbol{\sigma} \equiv [\sigma_0 \cdots \sigma_k \cdots \sigma_{L-1}]. \quad (2.3)$$

σ_k is the kernel size for the k -th feature.

Finally, the similarity distribution is written as

$$D_i(\mathbf{x}) = \sum_{j=0}^{M_i-1} \exp \left[-\frac{1}{2} \sum_{k=0}^{L-1} \left(\frac{x_k - \mu_{i,j,k}}{\sigma_k} \right)^2 \right] = \sum_{j=0}^{M_i-1} \exp \left[-\frac{1}{2} \frac{(\mathbf{x} - \boldsymbol{\mu}_{i,j})(\mathbf{x} - \boldsymbol{\mu}_{i,j})^T}{\boldsymbol{\sigma} \cdot \boldsymbol{\sigma}^T} \right]. \quad (2.4)$$

A similarity distribution vector is defined as

$$\mathbf{D}(\mathbf{x}) \equiv [D_0(\mathbf{x}) \cdots D_i(\mathbf{x}) \cdots D_{N-1}(\mathbf{x})]. \quad (2.5)$$

The similarity of the p -th pixel (\mathbf{S}_p) to each reference region is then given as

$$\mathbf{S}_p \equiv \mathbf{D}(\boldsymbol{\mu}_p) = [D_0(\boldsymbol{\mu}_p) \cdots D_i(\boldsymbol{\mu}_p) \cdots D_{N-1}(\boldsymbol{\mu}_p)], \quad (2.6)$$

where \mathbf{S}_p is an N -dimensional vector.

2.1.4 Display of the discrimination results

The similarity vector \mathbf{S}_p is then converted to red-green-blue values for the purpose of display.

The typical color of the i -th reference region of the i -th tissue type is arbitrarily determined and expressed as

$$\mathbf{C}_i = [R_i \ G_i \ B_i], \quad (2.7)$$

where R_i , G_i , and B_i are the red, green, and blue values of a pure i -th tissue. Namely, the respective color appears at a pixel that has the following similarity vector.

$$\mathbf{S}_p = [S_0 \cdots S_a \cdots S_{N-1}], \quad \text{where } S_a = \begin{cases} 1 & : a = i \\ 0 & : a \neq i \end{cases}. \quad (2.8)$$

According to this similarity vector, the color conversion matrix is defined as

$$\mathbf{A} \equiv [\mathbf{C}_0^T \cdots \mathbf{C}_i^T \cdots \mathbf{C}_{N-1}^T] = \begin{bmatrix} R_0 & \cdots & R_i & \cdots & R_{N-1} \\ G_0 & \cdots & G_i & \cdots & G_{N-1} \\ B_0 & \cdots & B_i & \cdots & B_{N-1} \end{bmatrix}. \quad (2.9)$$

This matrix is a $3 \times N$ matrix.

Finally, the RGB values of the p -th pixel in a discriminated OCT image is calculated as follows.

$$\mathbf{Q}_p = \mathbf{A} \mathbf{S}_p^T. \quad (2.10)$$

Although I already have a discriminated OCT image \mathbf{Q} , yet another visualization of the composition of a log-scale intensity OCT and the discriminated OCT, which is

referred to as a pseudo-color structural OCT, may be useful. The RGB value of the p -th pixel in the pseudo-color structural OCT is defined as follows.

$$\mathbf{R}_p \equiv \frac{\mathbf{Q}_p}{\mathbf{L} \cdot \mathbf{Q}_p^T} I_p, \quad (2.11)$$

where I_p is a logarithmically scaled OCT intensity of the p -th pixel. \mathbf{L} is a luma matrix

$$\mathbf{L} \equiv [0.299 \quad 0.587 \quad 0.114]. \quad (2.12)$$

$\mathbf{L} \cdot \mathbf{Q}_p^T$ is a luma of the discriminated OCT \mathbf{Q}_p .

2.1.5 3D tissue discrimination

I created a 3D volume consisting of 256 pseudo-color structural OCT images. These B-scans were discriminated by a single similarity distribution. Because of B-scan dependent intensity difference, feature values slightly vary between different B-scans. Hence, I selected 2 B-scans that have a larger difference in intensity and summed up the similarity distribution vectors created from these 2 B-scans. This summation is used as a unified similarity distribution vector for the discrimination of all B-scans of the volume. Namely, the similarity distribution is created only once for a 3D volume.

2.2 Results of tissue discrimination in anterior eye

Figure 2.1(a) shows images of the selected reference regions; the conjunctiva is shown in light brown; the sclera, in green; the TM, in dark yellow; cornea, in blue; and the uvea, in red. The pixels in the reference regions were then plotted in a 3D feature space of the intensity, extinction coefficient, and birefringence as shown in Fig. 2.1(b). The plotted colors in Fig. 2.1(b) are identical to the colors of the corresponding reference regions in Fig. 2.1(a). Feature distributions of the 5 reference regions were well separated in the 3D feature space. This indicates that the 3 parameters I used could successfully reflect the features of the target tissues.

The similarity distribution vector was calculated, and the final pseudo-color structural OCT image was created according to the method described above. I applied this method to 4 eyes of 4 subjects and similar discrimination results were obtained for all the eyes. Reference regions were selected for each subject. OCT images and discriminated results are shown in Fig. 2.2(a)-(d) and Fig. 2.2(e)-(h), respectively. I could observe different tissues with good contrast. The trabecular meshwork could be observed in the pseudo-color structural OCT image. The conjunctiva and sclera, which cannot be distinguished in conventional OCT images, could be clearly differentiated. However, although it is clinically not a significant error, a part of the cornea was discriminated as the uvea. This may be because the selected reference region of uvea does not fully represent the property of the entire uveal tissues. Additional features, e.g., optic axis orientations and degree-of-polarization uniformity, and the higher dimensional feature space that results from them might improve the specificity of tissue discrimination. Black regions in the pseudo-color structural OCT image represent no similarities to any reference regions. The borders and outliers are apt to become black due to the limit of our current algorithm.

A TM line as observed by gonioscopy can be observed in the 3D volume rendered pseudo-color structural OCT. Fig. 2.3(a) shows a gonioscopic image and corresponding

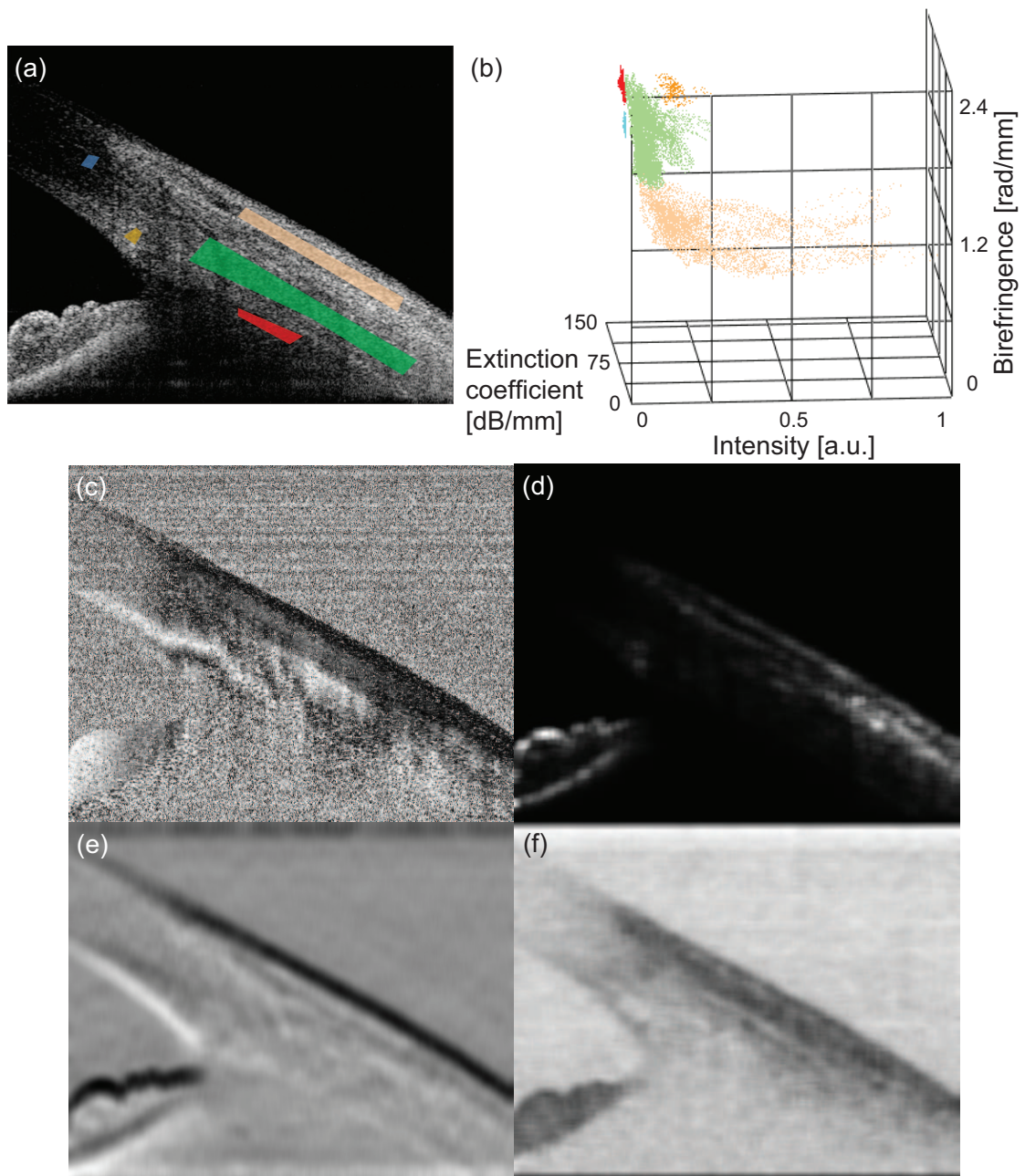


Figure 2.1: Feature distributions of the 5 reference regions in the 3D feature space. (a) The 5 reference regions (light brown, conjunctiva; green, sclera; dark yellow, TM; blue, cornea; red, uvea) studied in subject 1. They were selected manually on the basis of their anatomical and histological features; (b) Feature distributions of the 5 reference regions in the 3D (I-EC-BR) feature space. The corresponding phase retardation image (c), the OCT intensity in a linear scale (d), the extinction coefficient (e), and the birefringence (f) are also shown.

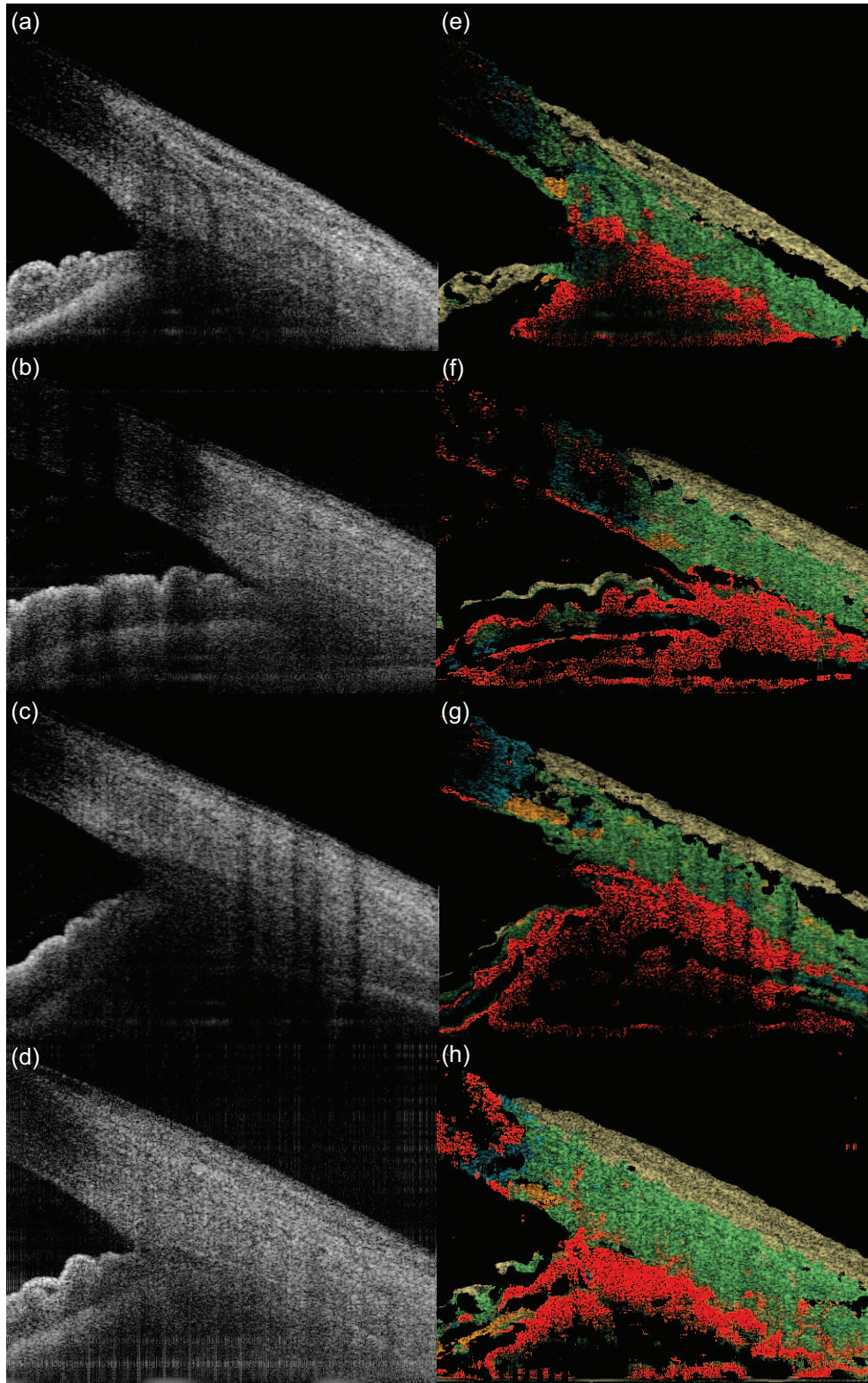


Figure 2.2: Results of the tissue discrimination. First column – OCT images of subject 1(a), 2(b), 3(c), and 4(d); second column – discriminated results of subject 1(e), 2(f), 3(g), and 4(h) displayed as a pseudo-color structural OCT. The light brown indicates conjunctiva, green indicates sclera, dark yellow indicates TM, blue indicates cornea, and red indicates uvea. Different tissues can be observed with good contrast and the trabecular meshwork can also be seen.

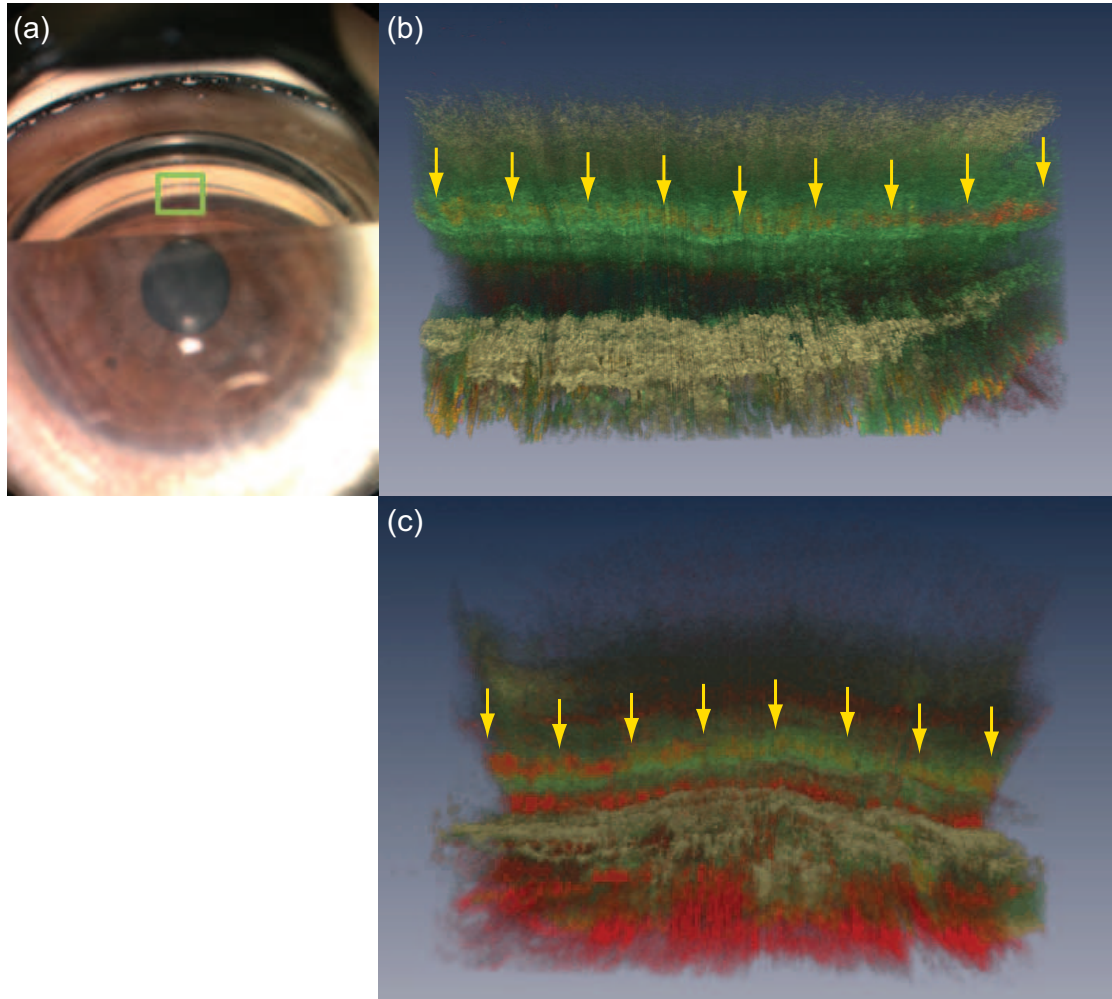


Figure 2.3: Gonioscopic images obtained by 3D discriminated volume. (a) Gonioscopic image of the right eye of subject 1 at 9 o'clock position. The image is rotated clockwise by 90 degrees. 3D discriminated volume of the (b) normal eye (1.9 MB and 6.0 MB movies) and (c) narrow angle eye (1.9 MB and 6.3 MB movies). These images correspond to the view of the green square in (a). TM can be observed as a yellow line as indicated by yellow arrows.

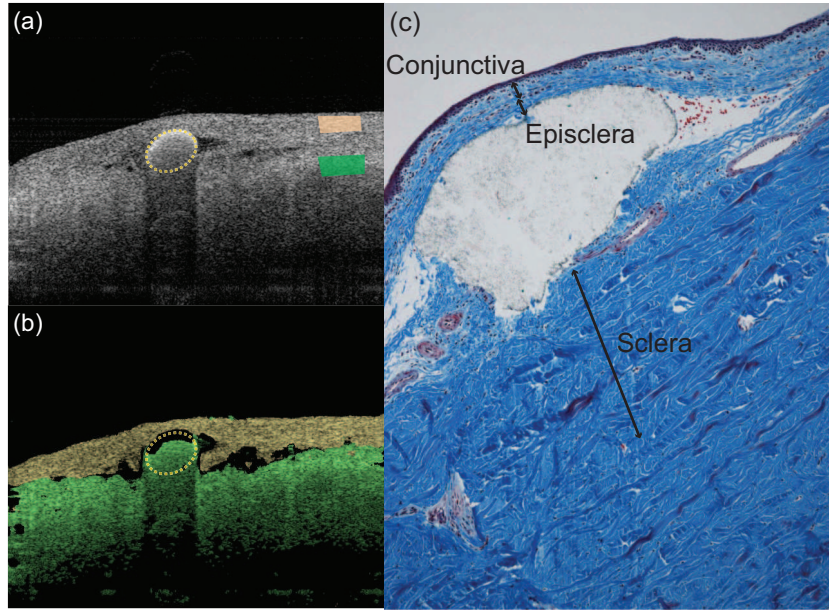


Figure 2.4: Validation of the tissue discrimination result with in vitro porcine eye. (a) Intensity image of the porcine eye. The marker (dashed line) was injected into sub-Tenon's space. The reference regions for the conjunctiva (light brown) and sclera (green) were selected manually. (b) Pseudo-color structural OCT. Tissues that were anterior to the marker (dashed line) and posterior to the marker were segmented. (c) Specimen of the porcine eye stained by Masson's trichrome method. The marker was injected into sub-Tenon's space. The anterior portion of the marker consists of the conjunctiva and episclera, and the posterior portion is identified as the sclera histologically.

view can be available from 3D volume as shown in Fig. 2.3(b) and (c). The TM line is observed between the cornea and uvea as indicated by yellow arrows. The pseudo-color structural OCT volumes of a normal eye (Fig. 2.3(b)) and a narrow angle eye (Fig. 2.3(c)) can be clearly differentiated. According to the distance between the TM and the surface of the iris, we can intuitively assess the angle structures. Our method is useful for investigating the narrow angle eye, and it might be useful for the screening of patients for angle-closure glaucoma. Because OCT is a non-contact measurement method, I can apply this method as a non-contact alternative to gonioscopy. This OCT-based non-contact gonioscopic investigation can be easily applied for studying a large number of patient for large-scale screening, and can be applied to all patients, including who have undergone surgery and are hence at a high risk of infections.

2.3 Discussions

2.3.1 Comparison with histological analysis

I validated this method by applying this algorithm and histological data to fresh in vitro porcine eyes. For this measurement, I injected a marker into sub-Tenon's space. It was injected with a 25G needle by an ophthalmologist. The marker injected was a thermo-plastic resin adhesive (solvent type, product number 195, CEMEDINE CO. LTD.). I examined the site of injection by PS-OCT and applied the discrimination algorithm. A representative pseudo-color structural OCT is presented in Fig. 2.4. OCT image and

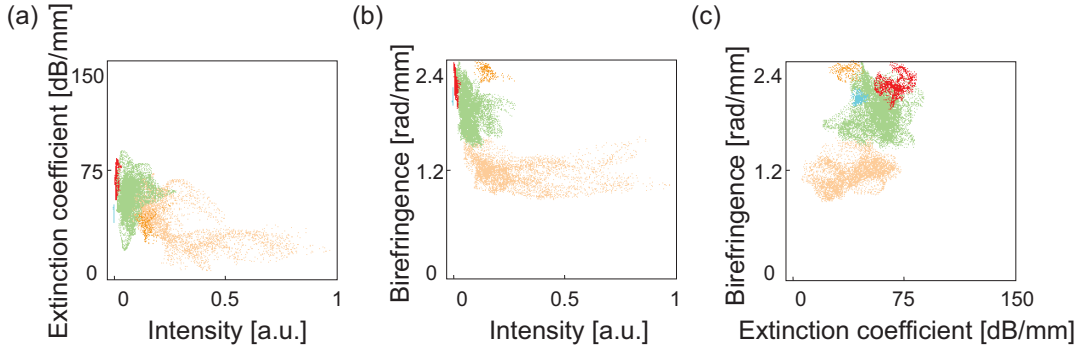


Figure 2.5: Feature distributions in the 2D feature spaces. (a) I-EC, (b) I-BR, and (c) EC-BR (light brown, conjunctiva; green, sclera; dark yellow, TM; blue, cornea; red, uvea). The 5 tissues could not be simultaneously discriminated by 1D or 2D analysis.

discriminated result are shown in Fig. 2.4(a) and (b), respectively. For this discrimination, I used 2 reference regions, which were selected from the conjunctiva and sclera. I found that the selection of these reference regions results in the discrimination of tissues that are anterior to the marker and posterior to the marker. The tissue was processed to formalin-fixed and paraffin-embedded block, and cut into $5\mu\text{m}$ -specimen. The specimen was stained by Masson's trichrome method, which stains collagen fiber blue, as shown in Fig. 2.4(c). According to the interpretations by a clinical ophthalmologist, an ophthalmic pathologist, and a pathology specialist, the marker was considered to be present in the region between the episclera and sclera. The episclera is the outermost layer of the sclera, which is a loose, highly vascular connective tissue, and is attached to Tenon's capsule. From this measurement, the region recognized as the conjunctiva according to this algorithm seems to include the conjunctiva itself, Tenon's capsule, and the episclera.

2.3.2 Advantage of 3D feature spaces

The feature distributions were well separated in 3D feature spaces. However, they could not be separated by 1D or 2D analysis. Feature distributions in 2D feature spaces are shown in Fig. 2.5. In the I-EC space, the TM overlapped the sclera and conjunctiva (Fig. 2.5(a)). This suggests that birefringence obtained by PS-OCT played a decisive role in identifying the TM. In the EC-BR space, it is observed that the extinction coefficient can effectively be used to differentiate between the cornea and uvea (Fig. 2.5(c)).

The separation among the reference regions are quantified by using their normalized distances. The normalized distance between the distributions of l -th and m -th reference regions in respect to n -th feature is defined as

$$\Delta_{l,m}^{(n)} \equiv \frac{|M_l^{(n)} - M_m^{(n)}|}{\sqrt{(SD_l^{(n)})^2 + (SD_m^{(n)})^2}} \quad (2.13)$$

where $M_l^{(n)}$ and $SD_l^{(n)}$ are the mean and the standard deviation of the distribution of l -th reference region in respect to n -th feature, respectively. $M_m^{(n)}$ and $SD_m^{(n)}$ are those of the m -th reference region. Subsequently, the normalized distance between the l -th and

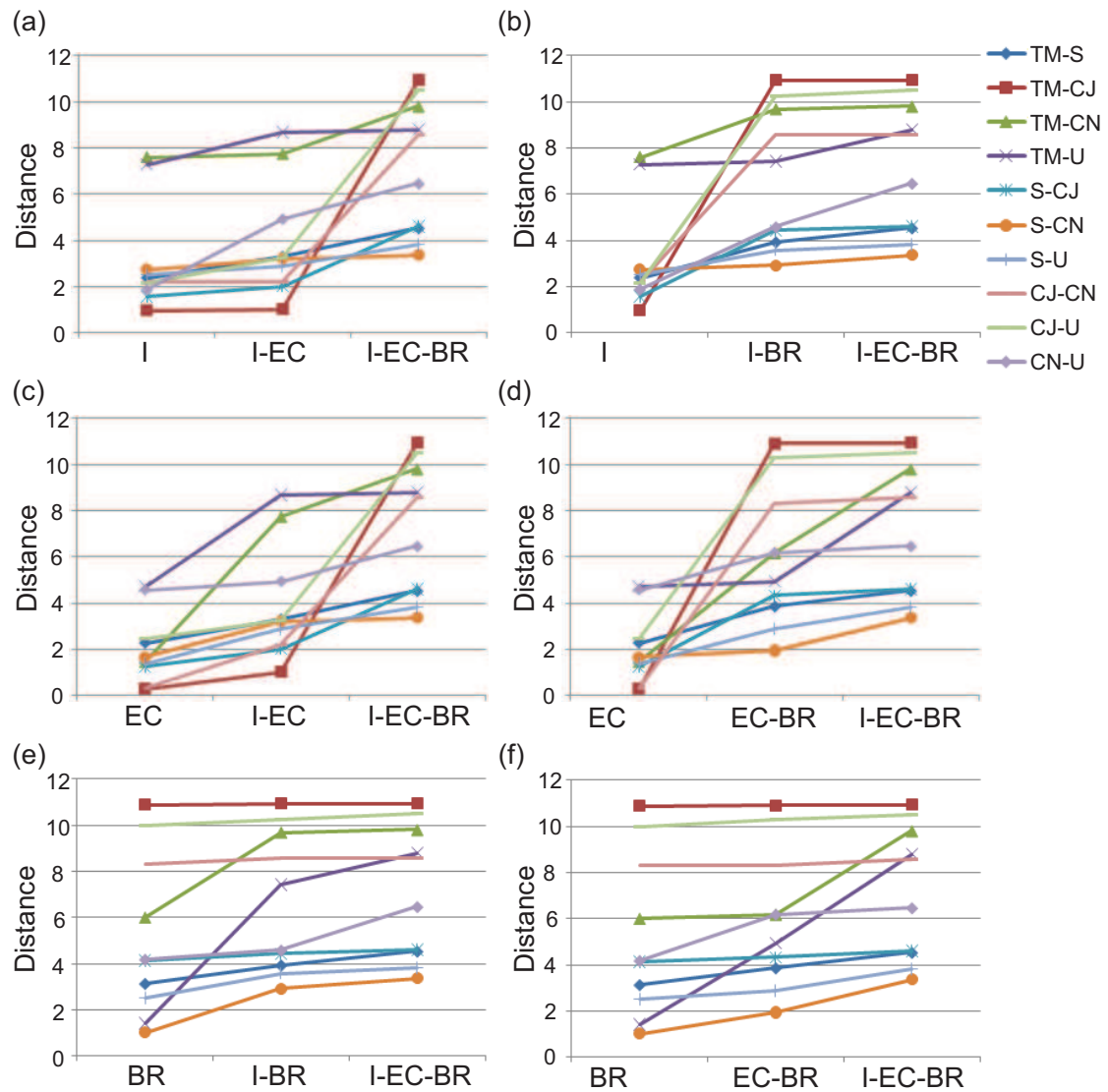


Figure 2.6: The normalized distances of all the pairs of the 5 reference regions in each feature space. The same dataset and the same reference regions with those of Fig. 2.1(a) were used. I: intensity, EC: extinction coefficient, BR: birefringence; TM: trabecular meshwork, S: sclera, CJ: conjunctiva, CN: cornea, and U: uvea.

m -th reference regions in the 2D feature space of the n -th and o -th features is defined as

$$\Delta_{l,m}^{(n,o)} \equiv \sqrt{\left(\Delta_{l,m}^{(n)}\right)^2 + \left(\Delta_{l,m}^{(o)}\right)^2}, \quad (2.14)$$

and that in the 3D feature space of the n -th, o -th and p -th features is defined as

$$\Delta_{l,m}^{(n,o,p)} \equiv \sqrt{\left(\Delta_{l,m}^{(n)}\right)^2 + \left(\Delta_{l,m}^{(o)}\right)^2 + \left(\Delta_{l,m}^{(p)}\right)^2}. \quad (2.15)$$

The normalized distances were obtained for all pairs of 5 reference regions in each 1D to 3D feature space as shown in Fig. 2.6, where the same dataset and the same reference regions with Fig. 2.1(a) were used. The horizontal axes represent the combination of the features and the vertical axes represent the normalized distance. The averaged normalized distance of all the pairs of reference regions was improved to be 7.14 in 3D feature space, while those in 1D feature spaces were 3.12, 2.03 and 5.15 for I, EC, and BR, respectively, and those in 2D feature spaces were 6.62 for I-BR, 3.92 for I-EC, and 5.97 for EC-BR. This analysis quantitatively indicates that the usage of a larger number of features provides better separation of reference regions. It is also noteworthy that all distances, except of the TM-uvea and the sclera-cornea, increased when the birefringence were involved as shown in Figs. 2.6(a)-(d). I also find that the introduction of extinction coefficient increases the distance between cornea and uvea effectively, as shown in Figs. 2.6(a)-(b) and 6(e)-(f).

2.3.3 Selection of the reference regions

In this current algorithm, the reference regions are manually selected. To make the result robust to the fluctuation of the selection of the reference regions, I employed the following maneuver.

First, except for the selection of TM, I selected a small reference region which was surely a part of the tissue of interest as shown in Figs. 2.7(a), (e), (i) and (m). Second, the operator monitored the similarity distribution obtained with the first small reference region as shown in the Figs. 2.7(b), (f), (j) and (n) (yellow regions). The operator then selected the second reference region to include the high similarity regions of the first similarity map. And this second reference region was used for the subsequent tissue discrimination analysis. This two-step selection protocol made this algorithm robust.

The reference region of TM was selected after the selection of the sclera. The similarity of the sclera showed a void region close to the scleral spur as indicated by a blue circle in Fig. 2.7(d). This region was then selected as the reference region of TM as shown in Fig. 2.7(q).

Figure 2.7(s) shows the final pseudo-color structural OCT image. This image and the image shown in Fig. 2.2(e) were created from the same dataset, but the reference regions were selected independently by a single operator with a time interval of one month. It is noteworthy that these two images show similar results despite the reference regions have been selected independently.

The automation of this selection procedure may increase the stability of the algorithm, and this may be a subject of a future development.

2.3.4 Error in BR measurement

In the Fig. 2.1(b), conjunctiva shows higher birefringence than expected. This relatively high birefringence is an artifact and comes from asymmetric distribution of BR in the

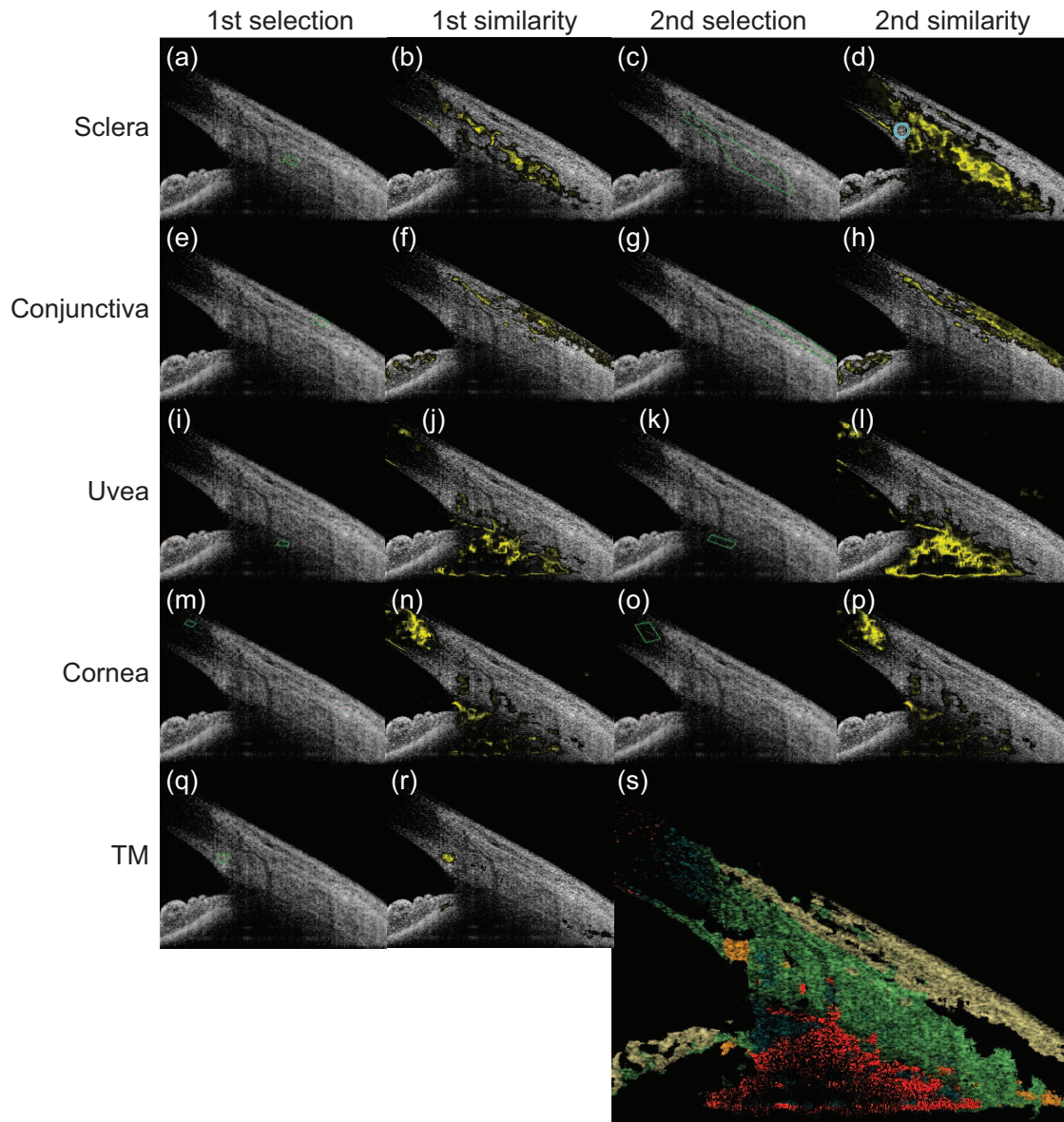


Figure 2.7: (a)-(r) An example of the selection of reference regions. The raw represents the tissue of interest. The first and second columns represent the reference regions selected in the first step, and similarities obtained from the first selected reference regions, respectively. The third and fourth columns represent the reference regions of the second, i.e. the final, step, and similarities obtained from this final selections. (s) A pseudo-color structural OCT image obtained by the reference regions indicated in (c), (g), (k), (o) and (q).

feature space.

Our PS-OCT algorithm is based on Jones matrix formalism and the range of phase retardation as well as BR is limited from 0 to 180 degrees. If the true BR is close to zero, as in the case of conjunctiva, additional noises shift some of BR values to the negative range, and then this negative BR value is aliased into the above mentioned positive range of 0 to 180 degrees [16,41,42]. This aliasing skews the distribution of the measured BR. Consequently, the window averaging of this skewed distribution provides a slightly up-shifted BR value. A similar and detailed discussion is described in Ref. 43.

2.4 Conclusions

I developed a tissue discrimination algorithm using 3 parameters of optical properties obtained by PS-OCT. This discrimination algorithm is not based on structural information, but directly on the properties of the tissues. The conjunctiva, sclera, TM, cornea, and uvea were well separated in the 3D feature space and could be successfully discriminated. In the 3D discriminated volumes, the TM line was clearly observed. Thus, the combination of 3 parameters enabled simultaneous discrimination of the 5 tissues. In particular, the birefringence obtained by PS-OCT played an important role in the discrimination of the TM.

Chapter 3

Improvement of tissue discrimination ability in posterior eye

Optical coherence tomography (OCT) possesses high resolution and high acquisition speed, and three-dimensional volumetric imaging and video rate monitoring capabilities. OCT has been applied in scientific, industrial, and medical fields [10, 44]. Particularly in ophthalmology, OCT has been widespread and is becoming an essential tool in the diagnosis and monitoring of human retinal disease [45].

An OCT signal intensity image provides layered structures of the retina and helps in the accurate diagnosis of retinal disease. Polarization sensitive OCT (PS-OCT) provides not only structural information but also the polarization properties of the sample [46, 47]. Among the polarization properties, local birefringence (BR) is considered to provide collagen contrast [48–55]. The degree of polarization uniformity (DOPU) is another polarization property [3, 4, 56, 57]. Low DOPU signal is considered to be an indicator of melanin [5]. OCT angiography (OCTA) is another extension of OCT, that provides vascular information through the time variation analysis of OCT signals [6, 7, 58, 59]. Jones matrix-based PS-OCT, the so-called multifunctional Jones matrix OCT (JM-OCT), provides the following four types of OCT images: scattering intensity, BR/phase retardation, DOPU, and OCTA using a single scan [8, 9, 52, 54, 60].

Local statistics are frequently used for the image processing of JM-OCT. For example, the local mean is used to reduce noise and speckle. Similarly, DOPU is computed as a circular variance of Stokes vectors in a local region [3]. BR is also estimated using signals in a small local region [50, 55]. Conventionally, these local statistics are computed using a fixed-size rectangular kernel. However, the fixed-size kernel results in a trade-off between image sharpness and statistical accuracy, that is, a larger kernel provides better statistical accuracy but reduces the image resolution.

I introduce clusters of pixels with a flexible shape, so-called superpixels, as the kernel for computing local statistics. A superpixel is formed with image pixels that share similar signal values and possess high spatial proximity [61]. Using the superpixel as the local statistics kernel, I can preserve tissue structures and simultaneously achieve accurate statistics.

In this study, I present a superpixel method that is based on the idea of the SLIC algorithm [62, 63] but is specially designed for multifunctional JM-OCT. The SLIC algorithm generates superpixels by clustering pixels based on their spatial proximity and

color similarity. Our JM-OCT superpixel method generates superpixels by clustering pixels based on their spatial proximity and optical feature similarity where the optical features include OCT intensity, BR, DOPU, and OCTA. The performance of JM-OCT superpixels is evaluated in detail for datasets obtained from *in vivo* human posterior eyes. Systemic methods for optimizing parameters used for superpixel generation are also presented.

3.1 JM-OCT system and measurement protocol

In this study, I used a multifunctional JM-OCT designed for posterior eye imaging [9]. A MEMS-based wavelength sweeping light source (Axsun Technology Inc., MA) with a center wavelength of $1.05 \mu\text{m}$ was used. The scanning rate of the light source was 100 kHz and the average output power was 30 mW. The optical power on the sample was configured to be approximately 1.15 mW to satisfy the safety standard defined by ANSI [64].

This JM-OCT multiplexed two incident polarization states using passive polarization delay, and two output polarizations were measured using a polarization diversity detector [5, 8, 9, 51, 52, 54]. Thus, it measured a set of four OCT images by a single scan. The four images formed a Jones matrix, which is a similarity transformed matrix of the round-trip Jones matrix of the sample. Additionally, four Jones matrix B-scans were repeatedly obtained at a single location on a sample. More details of this JM-OCT are described in Ref. [9].

Four types of optical features, OCT intensity, BR, DOPU, and OCTA, were then computed from the Jones matrix. OCT intensity was computed by coherently combining four entries of the Jones matrix and also combining four repeated Jones matrices [9]. BR was computed using a local Jones matrix analysis method [49] and maximum *a-posteriori* BR estimator [50]. DOPU was computed using a DOPU algorithm with Makita’s noise correction [4]. Additionally, OCTA was obtained by complex correlation analysis with noise-correction [7]. More details of the signal processing are summarized in Refs. [9, 52].

The sensitivity of each of the four images was measured to be 91 dB, which is equivalent to 97 dB for conventional non-polarization sensitive OCT [9]. The depth resolution was measured to be $8.5 \mu\text{m}$ in air, which corresponds to $6.2 \mu\text{m}$ in tissue. Each A-line consisted of 480 pixels, and the axial pixel separation was $4.0 \mu\text{m}$.

Maculae and optic nerve heads (ONHs) of two healthy human subjects were measured. Horizontal cross-sections were obtained with a 6.0 mm scan range laterally and 1.9 mm in depth. Sixty-four B-scans were obtained continuously, and each B-scan consisted of 490 A-lines. Four B-scans among the 64 were used for the analysis.

3.2 Generation and optimization of superpixels for JM-OCT

In this section, I first explain a method to generate superpixels from multi-contrast Jones matrix OCT images (Section 3.2.1). Then the methods and algorithms to optimize the parameters used to generate the superpixels are described in 3.2.2.

3.2.1 Superpixel generation

Generation of initial superpixels

A superpixel is a cluster of image pixels with high spatial proximity and high optical feature similarity. To generate superpixels, I first created initial superpixels that had a fixed size and hexagonal shape. They were regularly distributed in space and covered the entire image region. To generate the initial superpixel, I first selected the interval of initial superpixels S in a pixel unit. The number of superpixels K in an image with N image pixels is computed as $K = N/S^2$. Additionally, the number of pixels in each initial superpixel is S^2 . In the present study, S was set to six pixels, and hence the number of image pixels per superpixel was 36 pixels. The number of image pixels per image was 235,200 pixels (490×480 pixels), and hence the number of superpixels was 6,533/image.

Definition of distance in feature space

The initial superpixels were reshaped to increase both the optical feature similarity and spatial proximity of the image pixels in each superpixel. For this reshaping, I had to simultaneously evaluate the optical feature similarity and spatial proximity. So, I had to define an image pixel distance in six-dimensional (6-D) feature space, which consisted of four optical features (OCT intensity, OCTA, BR, and DOPU) and two spatial coordinates (lateral and axial).

The first step to define the 6-D distance was to define a distance in 4-D optical feature space. The optical feature distance between two image pixel points \mathbf{a} and \mathbf{b} is defined as the weighted Euclidean distance:

$$D_o(\mathbf{a}, \mathbf{b}) \equiv \sqrt{\sum_{i=1}^4 w_i (a_i - b_i)^2}, \quad (3.1)$$

where \mathbf{a} and \mathbf{b} are position vectors in the 6-D feature space, which can be expressed as $\mathbf{a} = [a_1, a_2, a_3, a_4, a_5, a_6]^T$ and $\mathbf{b} = [b_1, b_2, b_3, b_4, b_5, b_6]^T$. The first to fourth entries of the vectors represent the OCT intensity on a linear scale, OCTA, BR, and DOPU, respectively. The fifth and sixth entries are the lateral and axial spatial positions in the pixel unit. w_i is the weight of the i -th optical feature. A method to define an optimal w_i is described in Section 3.2.2. In this implementation, the optical feature values are normalized in the range of $[0, 255]$ and represented in floating point numbers in its software implementation. And it does not affect the final shape of the superpixels.

Similarly, the spatial distance is defined as the Euclidean distance:

$$D_s(\mathbf{a}, \mathbf{b}) \equiv \sqrt{\sum_{i=5}^6 (a_i - b_i)^2}, \quad (3.2)$$

Additionally, the total distance D_t in 6-D feature space is then defined as a weighted sum of the optical feature distance D_o and spatial distance D_s :

$$D_t(\mathbf{a}, \mathbf{b}) \equiv D_o(\mathbf{a}, \mathbf{b}) + \frac{m}{S} D_s(\mathbf{a}, \mathbf{b}), \quad (3.3)$$

where m is a weight between the optical feature distance and spatial distance. A larger m results in a larger contribution of spatial distance to total distance. As will be described

in the next subsection, the superpixel is reshaped to reduce D_t among pixels within a superpixel. Hence, a larger m results in more spatially compact superpixels, and m is called as the ‘‘compactness factor’’ [62]. A method to determine the optimal compactness factor is described in Section 3.2.2.

Superpixel reshaping

After generating the initial superpixels, they were reshaped in an iterative process similar to the SLIC superpixel method [62]. The reshaping was an iterative clustering process of image pixels in the 6-D distance D_t . For each iteration, the center of gravity of all the image pixels that belonged to each superpixel was computed in the 6-D feature space. This center of gravity is denoted as the centroid of the superpixel. The centroids of all superpixels were computed. Then each image pixel was reassigned to the superpixel whose centroid was the nearest to that image pixel. In this implementation, the searching area of the nearest superpixel was limited to within a $2S \times 2S$ area, which is double the interval of the initial superpixel, to accelerate the searching speed. The iteration continued until the superpixels converged into particular shapes. In practice, the iteration continued until the spatial distance between the previous and recomputed centroids became less than a threshold distance, which was 1 pixel in this study, or reached 10 iterations. This reassignment reshaped the superpixels to reflect the tissue structures.

After this iteration, some superpixels occasionally split into small fragments because this clustering process did not constrain spatial connectivity. Hence, after the convergence, small fragments of superpixels, that is, fragments smaller than four pixels in this study, were merged into the largest neighboring superpixel. This process is referred to as connectivity enforcement.

3.2.2 Optimization method of superpixel parameters

The superpixel method relies on some arbitrary defined parameters including the initial superpixel interval S , weights w_i , and compactness factor m . Among them, the initial superpixel interval is mainly defined based on the allowable computational load, while the weights and compactness factor should be optimized to make superpixels well adhere to tissue boundaries. In the following sections, I describe strategies and methods to optimize the weights (Section 3.2.2) and compactness factor (Section 3.2.2). To perform these optimizations, I requested quantitative metrics of the goodness of the superpixels. Thus, I first define the metrics in Section 3.2.2 before describing the optimization methods.

Intra-superpixel variance and contribution metric

I assumed that each type of tissue had a specific optical property. Thus, the measured optical feature values from the same tissue had similar values. If a superpixel adheres well to tissue boundaries and contains only a homogeneous tissue, the variance of the optical feature values within the superpixel should be low. Hence, the intra-superpixel variance (ISPV) of each optical feature can be considered as a metric to evaluate how well a superpixel adheres to tissue boundaries.

The variance of the i -th optical feature within the k -th superpixel is defined as

$$\sigma_{i,k}^2 = \frac{1}{s_k} \sum_{j=1}^{s_k} w_i (x_{i,j,k} - \bar{x}_{i,k})^2, \quad (3.4)$$

where s_k is the number of pixels within the k -th superpixel; w_i is the weight of the i -th optical feature, which is the same as that previously used for the distance calculation in Eq. (3.1); $x_{i,j,k}$ is the i -th optical feature value of the j -th pixel in the k -th superpixel; and $\bar{x}_{i,k}$ is the mean of the i -th optical feature values within the k -th superpixel.

I used the mean of all the variances within each superpixel as a metric for superpixel quality, which is referred to as the ISPV. The ISPV of the i -th optical feature V_i is expressed as

$$V_i \equiv \frac{1}{K} \sum_{k=1}^K \sigma_{i,k}^2, \quad (3.5)$$

where K is the number of superpixels in the image. Superpixels that adhere well to tissue boundaries obtained by the i -th optical feature should have low V_i .

Optimization of weights for the optical features

I used four optical features to discriminate tissue boundaries. Frequently, the boundary of a particular tissue is clearly delineated with some optical properties; however, this does not appear in other optical property images. For example, blood vessels are clearly visible in OCTA, but are barely visible in BR. Hence, if the superpixel shape is dominated by only a few optical properties, the superpixel does not follow the shape of tissues that appear only in the non-dominant optical properties. Thus, it is a rational optimization strategy to make the four optical properties equally contribute to superpixel formation. In this section, I present a method that controls the weights of the optical properties (w_i) so that all optical properties make an equal contribution.

In this optimization method, the contribution of the i -th optical property was evaluated using the following metric:

$$C_i \equiv \left(\frac{V_i^{reshaped}}{V_i^{initial}} \right)^{-1} = \frac{V_i^{initial}}{V_i^{reshaped}}, \quad (3.6)$$

where $V_i^{initial}$ and $V_i^{reshaped}$ are the ISPVs of the i -th optical property of the initial and reshaped superpixels, respectively. If an optical feature contributes to reshaping, the ISPV of the optical feature is reduced as the reshaping iteration progresses. Thus, ISPV may be useful as a measure of the contribution. However, ISPV is not directly usable for comparison among the optical features because each optical feature has different magnitudes of distribution. For example, a typical BR value of posterior eye tissue distributes approximately from zero to 6×10^{-3} , whereas a time correlation of OCT signals, which is a source of the OCTA signal, typically ranges from zero to one. Thus, the ISPVs of BR and OCTA are not directly comparable. To overcome this problem, the ISPV was normalized by the ISPV of the initial superpixel shape, as in the middle part of Eq. (3.6). I assumed that all the optical features were equally random within the initial uniform superpixels. Under this assumption, the normalized ISPV become comparable among the optical features. Finally, a contribution metric C_i is defined as the inverse of the normalized ISPV, that is, a greater contribution from an optical feature results in a higher contribution metric of the optical feature.

To equalize the contributions from the four optical features, the variance of the four contribution metrics was used as a cost function E :

$$E(\mathbf{w}) = \frac{1}{4} \sum_{i=1}^4 \left(C_i(w_i) - \frac{1}{4} \sum_{i=1}^4 C_i(w_i) \right)^2, \quad (3.7)$$

where $C_i(w_i)$ is a contribution metric of the i -th optical feature when the weight of the optical feature is w_i and \mathbf{w} is a vector of weights defined as $\mathbf{w} \equiv [w_1, w_2, w_3, w_4]^T$. As the contribution of all the optical features becomes more equal, $E(\mathbf{w})$ becomes smaller. Thus, the optimization of weights was performed to minimize $E(\mathbf{w})$.

I used an iterative method to minimize the cost function. The initial weights were determined randomly and the initial weight vector $\mathbf{w}^{(0)} = [w_1^{(0)}, w_2^{(0)}, w_3^{(0)}, w_4^{(0)}]^T$ was normalized to a unit vector. Hereafter, a superscript in brackets represents an iteration index. A new weight vector in the $(l + 1)$ -th iteration is then defined to be

$$\mathbf{w}^{(l+1)} \propto \mathbf{w}^{(l)} + \alpha \mathbf{d}^{(l)}, \quad (3.8)$$

where α was a step length, which controls the optimization speed. It was set to be 0.315 in this study. $\mathbf{d}^{(l)}$ is an update of the weight vector defined as

$$\mathbf{d}^{(l)} \equiv - \left[\mathbf{C}^{(l)} - \max \left\{ \mathbf{C}^{(l)} \right\} \right], \quad (3.9)$$

where $\mathbf{C}^{(l)}$ is a vector of contribution metrics at the l -th iteration defined as $\mathbf{C}^{(l)} = [c_1^{(l)}, c_2^{(l)}, c_3^{(l)}, c_4^{(l)}]^T$. $\max \left\{ \mathbf{C}^{(l)} \right\}$ is the maximum entry of $\mathbf{C}^{(l)}$. $\mathbf{w}^{(l+1)}$ is then normalized to a unit vector. Thus, Eq. (3.8) sufficiently specifies $\mathbf{w}^{(l+1)}$, although it is in a proportional form. The weights of the optical features with smaller contributions were increased more in the iteration. This iteration continued until $E(\mathbf{w})$ become smaller than 10^{-6} or reached 20 iterations.

Optimization strategy of the compactness factor

The compactness factor, m in Eq. (3.3), controls the balance between optical feature similarity and spatial proximity. If the compactness factor is too large, superpixels are not reshaped flexibly and remain almost in their initial hexagonal shape. If it is too small, the superpixels ignore spatial proximity and split into small fragments more frequently. In this case, the small fragments are absorbed into the largest neighboring superpixel in the connectivity enforcement step (as described in the last paragraph of Section 3.2.1). This connectivity enforcement ignores optical feature similarity, and hence, superpixels do not adhere to tissue boundaries well and the ISPV increases.

I had to determine an optimal compactness factor that might provide small ISPVs for all the optical features even after the connectivity enforcement. I optimized the compactness factor to minimize the normalized ISPVs of all the optical features, where the normalized ISPV is normalized by the ISPV of the initial superpixels. Recall that the normalized ISPV is the reciprocal of the contribution metric C_i , and the C_i s of all the optical features are nearly the same after optimizing the features' weights, as described in Section 3.2.2. Thus, the ISPVs of all optical features became similar to each other. I selected a compactness factor so that the average of the ISPVs of all the optical features (mean normalized-ISPV) had a minimum value. Superpixels with a lower mean normalized-ISPV can be considered to adhere to tissue boundaries better. This optimization was performed by brute force optimization, as described in Section 3.3.1.

Flow of optimizations

The entire optimization process is a three-level-nested iterative process, as summarized in Fig. 3.1. The outermost iteration optimizes the compactness factor (solid red box in

Fig. 3.1) and corresponds to Section 3.2.2. The second-level iteration is within this outermost iteration and optimizes the weights of the optical features (dashed green box, Section 3.2.2). The second-level iteration contains the innermost iteration, which is for superpixel generation (dashed and dotted blue box, Section 3.2.1).

3.3 Validation of the superpixel in posterior eye

This section consists of two subsections. In the first subsection (Section 3.3.1), I present the validation results of the optimization method of superpixel parameters. In the second subsection (Section 3.3.2), I present applications of superpixels to *in vivo* posterior eye images.

3.3.1 Validation of the superpixel parameter optimization methods

Validation of feature weights optimization

I searched for the optimal weights as described in Section 3.2.2. Fig. 3.2 shows examples of the weights of each optical feature as functions of the index of the optimization iteration. The three graphs show three trials (trial-1 to -3) of optimization, which were performed for the same ONH image, but started from different random initial weights. The compactness factor was set to five, which was found to be the optimal compactness factor as described in the next subsection. The weights of each optical feature converged after approximately 10 iterations and the converged values of the three trials were almost the same.

Fig. 3.3(a) shows the cost function $E(\mathbf{w})$ of trial-1 at each iteration. It is evident that the cost function successfully became very low and stable after a few iterations. The cost function became smaller than 0.01 after two iterations as shown in Fig. 3.3(b). The corresponding contribution metrics of each optical feature are shown in Fig. 3.3(c), where the colors of the plots of each feature are the same as those in Fig. 3.2. The contribution metrics of all features were successfully converged to a similar value after a few iterations. Thus, all the optical features equally contributed to superpixel formation with the optimized weights.

The optimal weight values varied among the measured tissue types, subjects, and measurement sessions. This issue will be discussed in Section 3.5.2.

Validation of the compactness factor optimization

Fig. 3.4 shows how the compactness factor (m) affected superpixel reshaping. The first column shows kernel-averaged OCT intensity images created using the superpixels as averaging kernels, and the second column shows superpixel images, where each superpixel is displayed in a randomly selected color. The weights of the optical features were optimized as described in Section 3.2.2 for each compactness factor. All superpixels generated with the compactness factor of 100 retained their initial hexagonal shape, even after reshaping [Fig. 3.4 (k)]. By contrast, the superpixels generated with the compactness factor 5 had a variety of shapes and sizes, and they adhered to the layered structure of the retina [Fig. 3.4 (q)]. Generally, I found that the reshaping flexibility of the superpixels increased as the compactness factor decreased. The mean normalized-ISPVs were 0.86, 0.80, 0.67, and 0.55 for $m = 100, 70, 40,$ and $5,$ respectively.

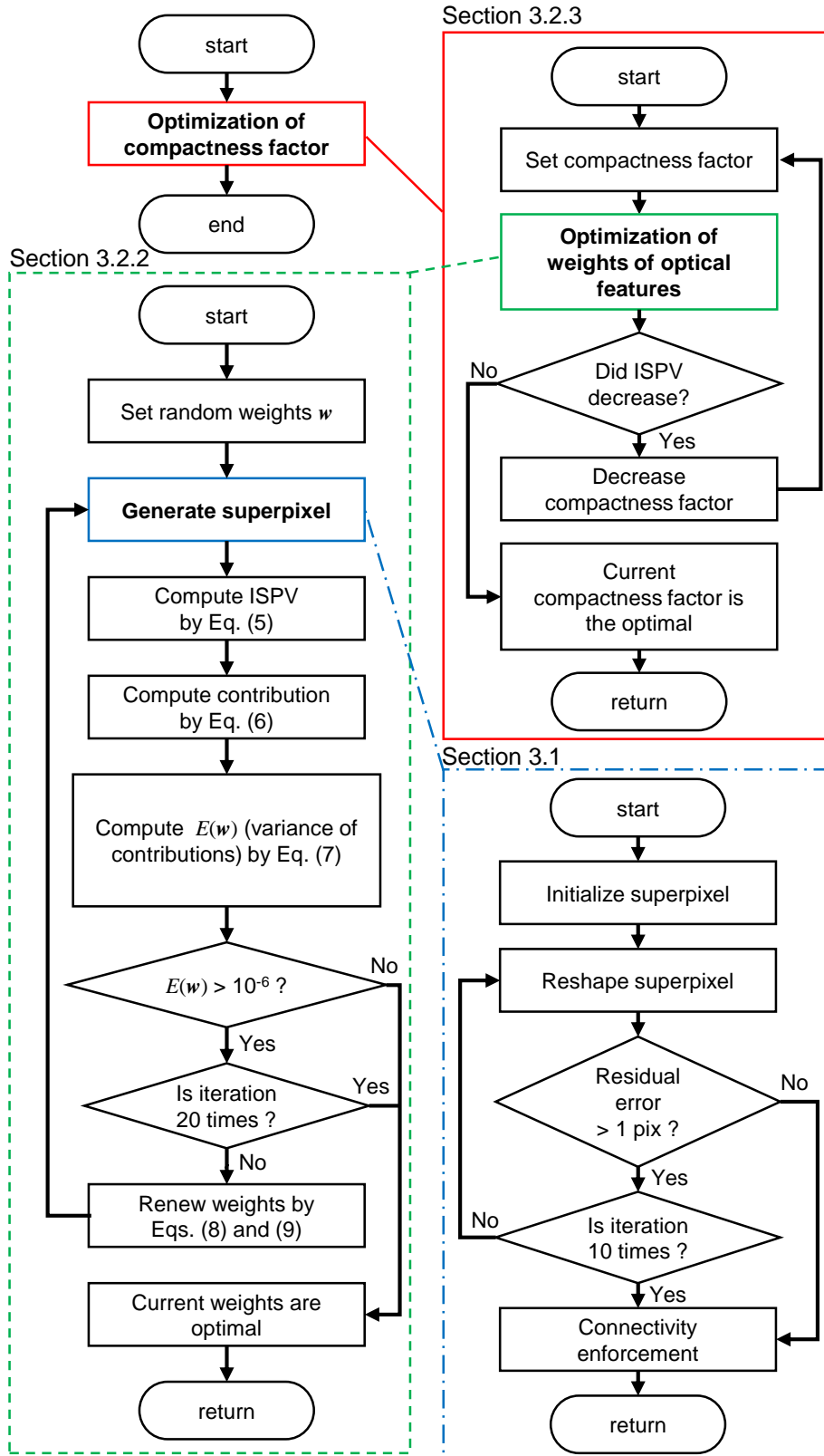


Figure 3.1: Flow of optimization for parameters used in superpixel generation. The parameters to be optimized include the compactness factor and weights of the optical features. Three loops are nested in the optimization process: the solid red, dashed green, and dashed and dotted blue boxes indicate the loops for compactness factor optimization (Section 3.2.2), weight optimization, (Section 3.2.2), and superpixel generation (Section 3.2.1), respectively.

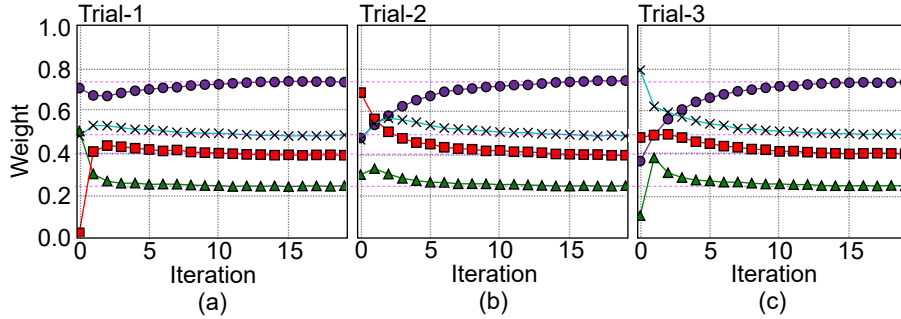


Figure 3.2: The alteration of the weights of the optical features during iterative optimization in three trials. (a) to (c) correspond to the first to third trials, respectively. Each plot color represents each optical feature as OCT intensity (purple, circle), OCTA (green, triangle), BR (red, square), and DOPU (blue, cross).

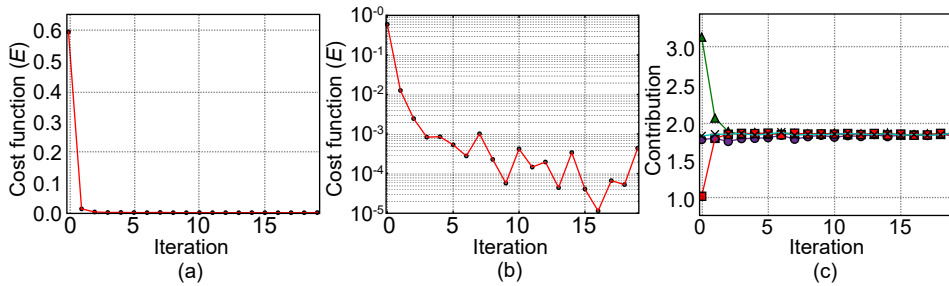


Figure 3.3: (a) The alterations of the cost function $E(\mathbf{w})$, (b) the logarithm of (a), and (c) the contribution metrics of each optical feature during the iterative optimization of the weights in the first trial. Each plot color in (c) represents each optical feature as OCT intensity (purple, circle), OCTA (green, triangle), BR (red, square), and DOPU (blue, cross).

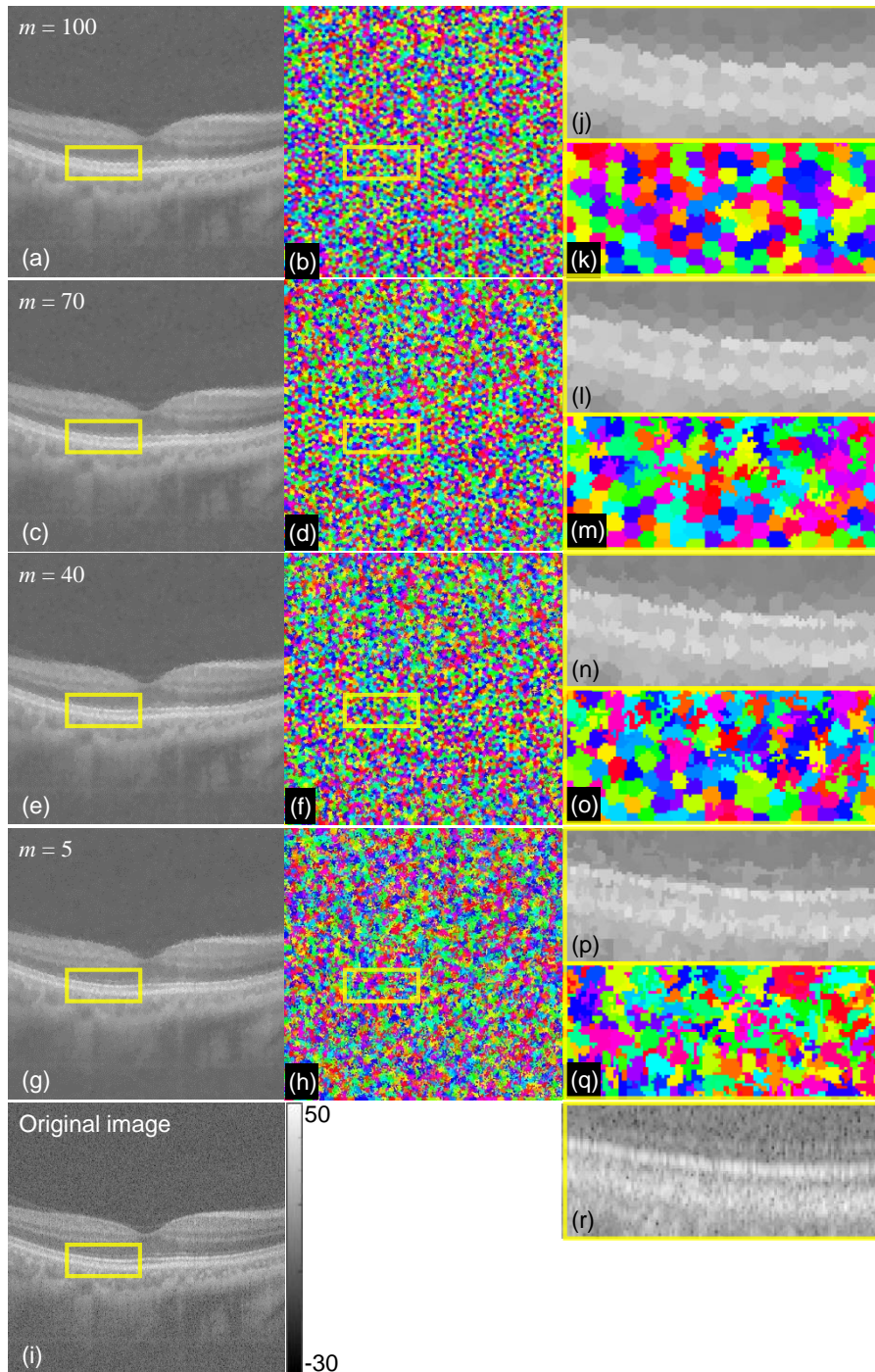


Figure 3.4: Superpixels generated with several compactness factor configurations. The first column ((a), (c), (e), and (g)) shows the kernel-averaged images with superpixel kernels. The second column ((b), (d), (f), and (h)) shows the superpixels where each superpixel is displayed with randomly assigned colors. The third column ((j)–(r)) shows magnified images of the images in the first and second columns, where the magnified regions are indicated by yellow boxes. Each row corresponds to the compactness factor of 100, 70, 40, and 5. The bottom row ((i) and (r)) shows the original (non-superpixelized) OCT intensity images.

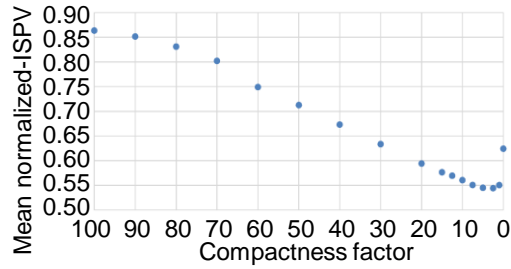


Figure 3.5: Mean normalized-ISPVs for several compactness factor configurations.

Fig. 3.5 shows an example of the mean normalized-ISPVs at each compactness factor, where a better compactness factor demonstrates a smaller mean normalized-ISPV. The mean normalized-ISPVs were computed from the same ONH image as that in Section 3.3.1, and the feature weights were optimized for each compactness factor independently. Generally, the mean normalized-ISPV decreased as the compactness factor decreased. This is because the lower compactness factor that reshapes superpixels is more highly dependent on optical feature similarity than spatial proximity. However, the mean normalized-ISPV increased if the compactness factor become too small. This can be explained as follows: A compactness factor that is too small results in a severe spatial fragmentation of superpixels at first, and then the small fragments are merged into the largest neighboring superpixels in the connectivity enforcement process. Because this merging is performed irrespective of the optical feature similarity, the mean normalized-ISPV becomes large.

I performed this evaluation for two retinal locations (macula and ONH) of two subjects, and found that a compactness factor of five always provided the minimal or nearly minimal normalized-ISPV. Thus, the compactness factor was set to five to obtain the results of Sections 3.3.1 and 3.3.2.

3.3.2 Superpixelization of *in vivo* posterior eye image

Fig. 3.6 shows an example of an ONH. The superpixels were generated with optimal feature weights, which were 0.7421 for intensity, 0.2392 for OCTA, 0.3930 for BR, and 0.4873 for DOPU. The compactness factor was set to five. The final mean normalized-ISPV was 0.547.

By observing the magnified images of OCT intensity [Fig. 3.6(i), (j), (k)], it is evident that the retinal layer structures that included retinal pigment epithelium (RPE) were well preserved by the reshaped superpixels. The shape of RPE can also be clearly recognized in the superpixelized DOPU image [Fig. 3.6 (t)]. Vessels in OCTA were clearly delineated by superpixels [Fig. 3.6(n)]. In the superpixelized BR image, high BR regions of sclera were depicted in the superpixelized BR image [Fig. 3.6(q)]. Thus, the superpixels were correctly reshaped to represent the tissue structures.

Fig. 3.7 shows an example of a macula, where the alignment of subfigures are the same as those in Fig. 3.6. The optimized feature weights were 0.6912 for OCT intensity, 0.3128 for OCTA, 0.4073 for BR and 0.5083 for DOPU, while the compactness factor was set to five. Similar to the case of the ONH, it can be seen that the reshaped superpixels well adhered to the tissue boundaries.

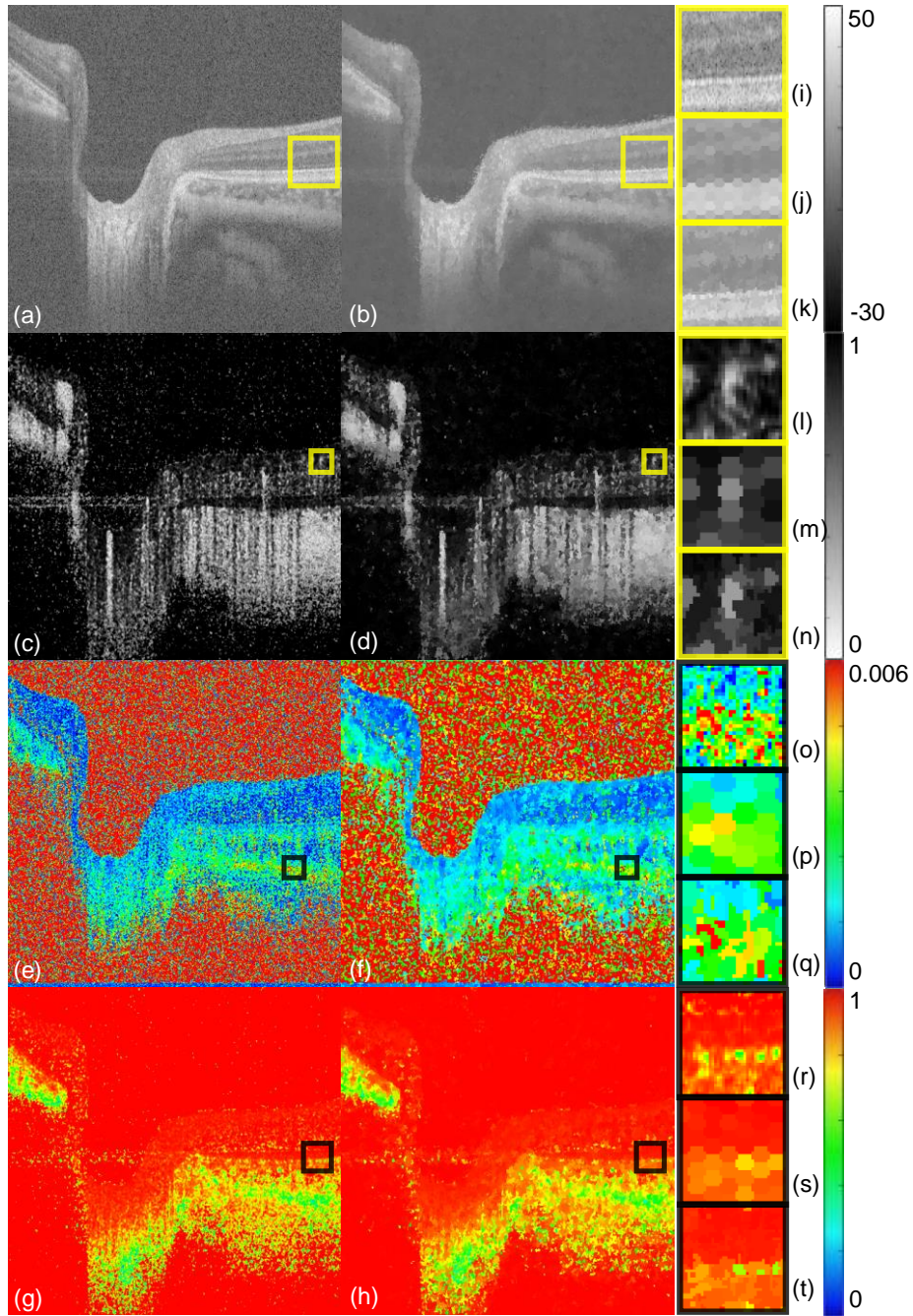


Figure 3.6: An example of an ONH. The first column shows the original images of (a) OCT intensity, (c) OCTA, (e) BR, and (g) DOPU. The second column ((b), (d), (f), and (h)) shows the kernel-averaged images with reshaped superpixels that correspond to the images in the first column. (i)–(k), (l)–(n), (o)–(q), and (r)–(t) show three types of images in the square windows in (b), (d), (f), and (h), respectively; (i), (l), (o), and (r) show the original images; (j), (m), (p), and (s) show the kernel-averaged images with initial (hexagon) superpixels; and (k), (n), (q), and (t) show the kernel-averaged images with reshaped superpixels.

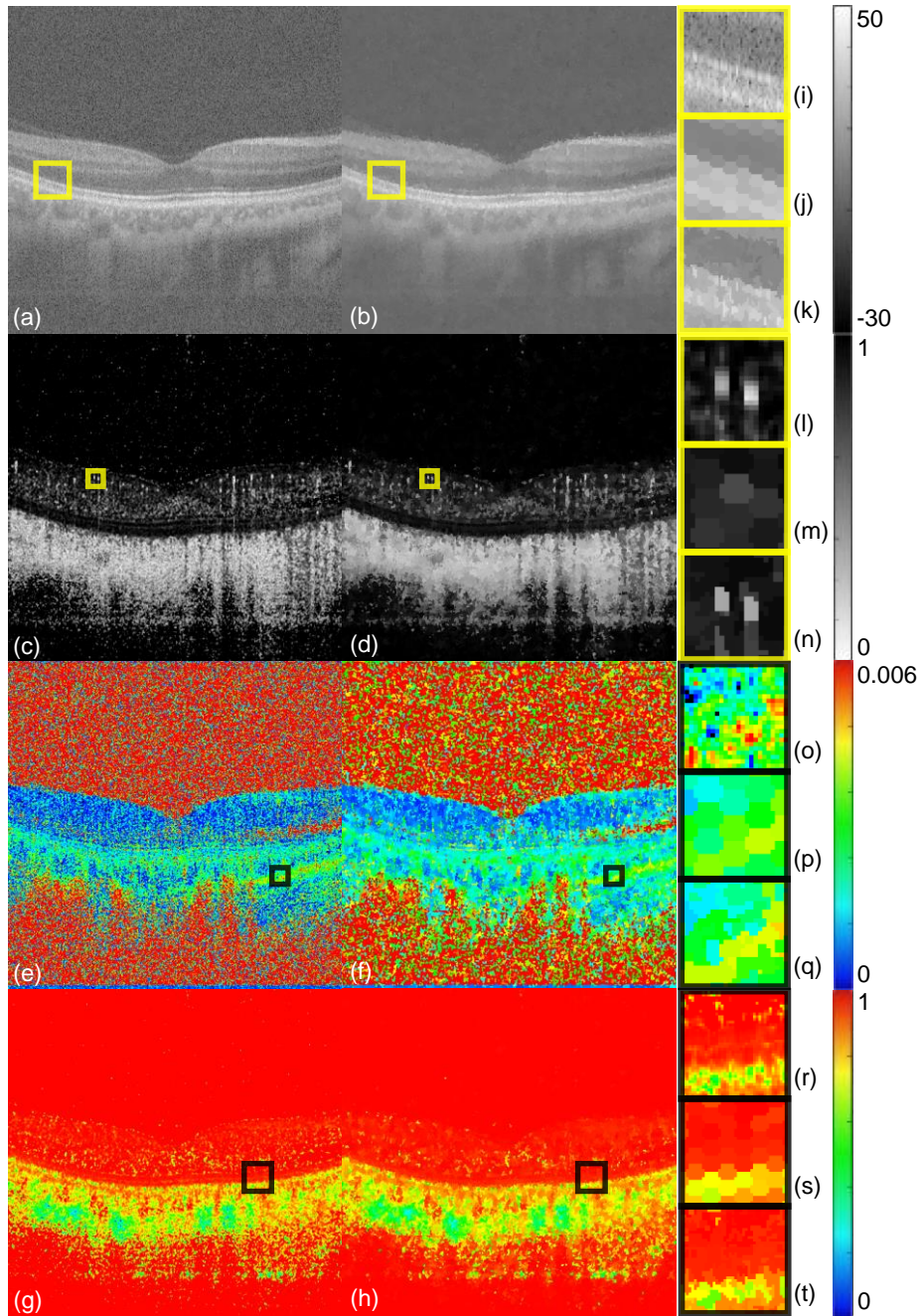


Figure 3.7: An example of a macula. The first column shows the original images of (a) OCT intensity, (c) OCTA, (e) BR, and (g) DOPU. The second column ((b), (d), (f), and (h)) shows kernel-averaged images with reshaped superpixels. The square boxes in (b), (d), (f), and (h) show the locations of (i)–(k), (l)–(n), (o)–(q), and (r)–(t). (i), (l), (o), and (r) show the magnified original images; (j), (m), (p), and (s) show the kernel-averaged images with initial (hexagon) superpixels; and (k), (n), (q), and (t) show the kernel-averaged images with reshaped superpixels.

3.4 Birefringence estimation using superpixel kernel in posterior eye

Retinal nerve fiber layer (RNFL) and lamina cribrosa are birefringent tissue and highly associated with glaucoma. So, quantitative analysis of birefringence of these tissues is useful. Jones matrix optical coherence tomography (JM-OCT) measures four optical properties of tissue; scattering, birefringence, the degree of polarization uniformity, and OCT angiography. Recently, high-accuracy birefringence measurement became available by using the maximum a posteriori (MAP) estimator. This estimator uses a certain spatial area, called as a kernel. Conventionally, the kernel is a uniform-shaped rectangle. It should be noted that if the kernel contains tissue boundary, the estimator cannot provide accurate birefringence. Here I introduce a new flexible kernel which has various shape and size to adhere to the tissue structure. It is combined with the MAP estimator and enables accurate birefringence estimation.

I utilized a custom made JM-OCT with 1.06-m probe. In this flexible kernel generation algorithm, whole image pixels are clustered as superpixels based on spatial proximity and similarity of the four optical features obtained by JM-OCT. For this clustering, the birefringence values estimated with a rectangle kernel is used. After generating the superpixel, I computed better estimation using the superpixel as the estimation kernel. Three eyes of 3 subjects were measured.

Higher contrast between the nasal NFL and other retinal layers is observed with the superpixel kernel than the rectangle kernel as shown in Fig. 3.8. I manually selected two regions of interest (ROIs) at the NFL and around inner plexiform layer. In all of the 3 eyes, the Bhattacharyya distances (histogram distance) between these ROIs with superpixel kernel were larger than those with rectangle kernel ($p = 0.0050$, Students t-test).

3.5 Discussions

3.5.1 Optimal definition of spatial distance

The pixel size of the images in this study was $4.0 \mu\text{m}$ (axial) \times $12.5 \mu\text{m}$ (lateral). Additionally, the spatial distance was expressed as the multiplication of the pixel size in the superpixel generation algorithm. Hence, the weight of the axial distance was approximately three times larger than that of the lateral distance. According to the final superpixel images, this imbalance between the weights of the spatial distances was acceptable. This could be partially because the retina has a layered structure, and hence it would be reasonable to apply a larger weight to the axial direction, which consists of a finer structure, than to the lateral direction.

3.5.2 Universality of the optimized weights of the optical features

In this algorithm, the weights of the four optical features were optimized for a specific single B-scan using the methods described in Section 3.2.2. I discuss how universally a specific set of weights optimized by a single B-scan is applicable to other B-scans. Universality is important because if the parameter set is universal, to some extent, the optimization is required only once for some range of B-scans. I discuss three types of universality. The first is intra-dataset universality, which is universality of the optimized weights among B-scans continuously obtained by a single measurement. The

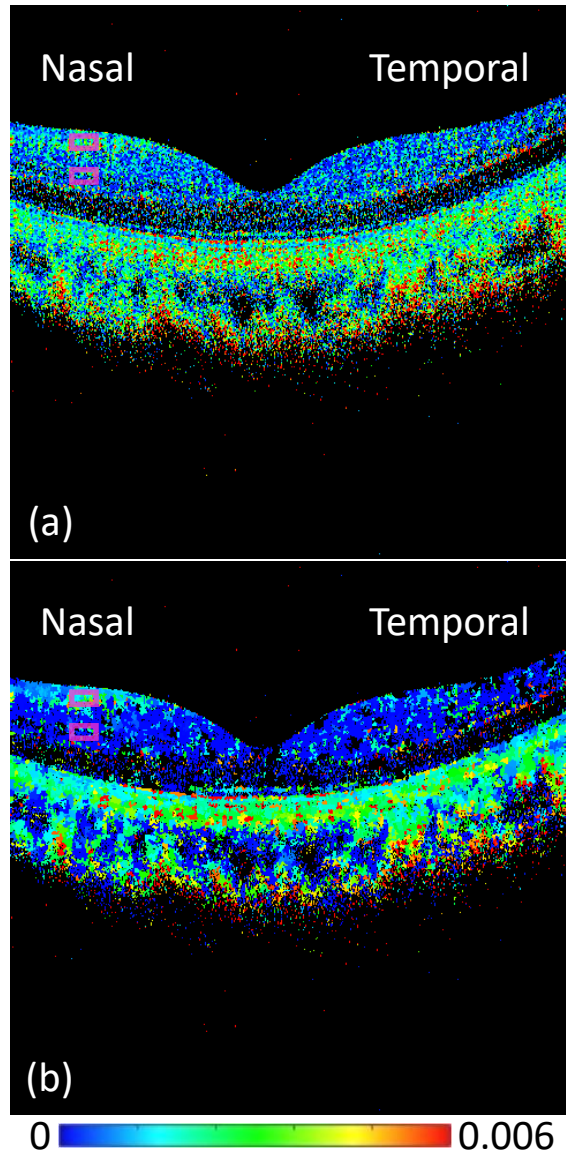


Figure 3.8: Birefringence of the macula with (a) rectangle kernel and (b) superpixel kernel. Purple rectangles indicate selected ROIs.

second is inter-dataset and intra-subject universality, where the weights are optimized and reapplied to datasets of the same subject but of different measurements. The third is inter-subject universality, which is the applicability of the optimized weights to a dataset from a different subject.

Optimization was performed to make the four optical features equally contribute to superpixel generation. Hence, the variance of the contributions among the optical features was used as a metric to evaluate the eligibility of a weight set, where the contribution is a quantity C_i defined by Eq. (3.6). This variance of the contributions becomes small if the weights are eligible for the B-scan. I consider that a set of weights is qualified to apply to a B-scan if the variance of the contributions is smaller than 0.01. As a reference, in Fig. 3.3 (c), the variance of the contributions became smaller than 0.01 after two iterations (0.592, 0.0126, and 0.00245 at the zeroth, first, and second iterations, respectively).

Additionally, the normalized-ISPV should be small for all optical features if the weights are eligible. Thus, the largest normalized-ISPV among the four optical features was used as a second metric to evaluate the weight set. A smaller maximum normalized-ISPV indicates that the weight set is more eligible for the B-scan. As a reference, I also generated superpixels without optimization because all weights were set to unity, and compared the normalized-ISPV to the optimized cases.

I computed these two metrics for B-scans taken from four ONHs and four maculae of four subjects and evaluated the three universalities. All subjects were 30 to 40 years old East Asians. Subjects 1 and 2 are the same subjects as those in the previous sections.

To evaluate the intra-dataset universality, I computed a set of optimal weights from a B-scan (training B-scan) and applied it to the other 3 B-scans (test B-scan) taken with the same acquisition sequence as the training B-scan. The results of the ONH are shown in Table 3.1. The variances of the contributions were smaller than 0.01 (qualified) for all test B-scans. All the largest normalized-ISPVs were also smaller than those without optimization; that is, all the largest normalized-ISPVs of the test B-scans with optimization were smaller than 0.578 and those without optimization were larger than 0.673. The normalized-ISPV was evidently improved by optimization. The same comparisons were performed in the macula, and the results are shown in Table 3.2. As with the ONH, the variances of the contributions were smaller than 0.01 for all test B-scans and the largest ISPVs were also smaller than those without optimization for all test B-scans. Hence, the optimal parameters can be considered to work well in other B-scans of the same measured volume.

Optimal weights of Training B-scan 1 in Table 3.1 and Table 3.2 were {I: 0.7968, OCTA: 0.2068, BR: 0.3452, DOPU: 0.4505} and {I: 0.7794, OCTA: 0.2797, BR: 0.3660, DOPU: 0.4245}, respectively.

For the evaluation of the inter-dataset and intra-subject universality, I first computed optimal weights from a B-scan (training B-scan), and applied it to a test B-scan, which was taken from another measurement session, but the same subject. The results were also compared with those with unoptimized results, where all the weights were set to unity. The same tests were performed for three subjects. The results of the ONH are summarized in Table 3.3, where VOC denotes variance of the contributions and nISPV denotes normalized ISPV. The variances of the contributions were smaller than 0.01 in all test B-scans and the largest ISPVs were also smaller than those without optimization for all test B-scans. The same comparisons were performed in the macula, and the results are shown in Table 3.4. The variances of the contributions were smaller than 0.01 for all test B-scans. However, the largest ISPV of test-3 with optimization was

Table 3.1: Validation for intra-dataset universality examined with an ONH of subject-1.

	Training B-scan 1	Test-1 B-scan 2	Test-2 B-scan 3	Test-3 B-scan 4
Variance of contributions	0.000111	0.00286	0.00377	0.00523
Largest normalized-ISPV with optimal weights	0.551	0.569	0.578	0.572
Largest normalized-ISPV without optimization	0.684	0.684	0.673	0.772

Table 3.2: Validation for intra-dataset universality examined with a macula of subject-2.

	Training B-scan 1	Test-1 B-scan 2	Test-2 B-scan 3	Test-3 B-scan 4
Variance of contributions	0.0000700	0.00206	0.00221	0.00404
Largest nISPV with optimal weights	0.553	0.589	0.581	0.593
Largest nISPV without optimization	0.648	0.662	0.655	0.668

0.609, and was not substantially improved compared with that without optimization (0.627). I conclude that there was inter-dataset and intra-subject universality, to some extent; however, it was not always the case. Thus, it would be safe to optimize the weights for each individual measurement dataset.

Training-1 in Table 3.3 and Table 3.4 were the same as the Training in Table 3.1 and Table 3.2, respectively. Optimal weights of Training-2 and Training-3 in Table 3.3 were {I: 0.7991, OCTA: 0.2189, BR: 0.3412, DOPU: 0.4438} and {I: 0.8390, OCTA: 0.2091, BR: 0.3001, DOPU: 0.4027}, respectively. Those in Table 3.4 were {I: 0.6452, OCTA: 0.3843, BR: 0.4104, DOPU: 0.5172} and {I: 0.6231, OCTA: 0.3320, BR: 0.4827, DOPU: 0.5180}.

For the inter-subject universality evaluation, I computed the optimal weights from a B-scan (training data) and applied them to the three B-scans (test data) of the other three subjects. I also computed the largest normalized-ISPV with unoptimized weights, all weights were set to unity for comparison. The results of the ONH are summarized in Table 3.5, where VOC denotes variance of the contributions and nISPV denotes normalized ISPV. The variances of the contributions were smaller than 0.01 in all test B-scans and the largest ISPVs were also smaller than those without optimization in all test B-scans. The same comparisons were performed in the macula, and the results are shown in Table 3.6. The variances of the contributions of Test-1 and Test-2 were larger than 0.01. The largest ISPV of Test-2 with optimization was 0.614, and was not substantially improved compared with that without optimization (0.641). Hence, I conclude that a set of optimized weights did not always work well in B-scans of other subjects. This lower universality among subjects could be partially explained by the inter-subject variation of the optical parameters of tissues. For example, the melanin concentration in choroid varied by age, which results in age-related variation of DOPU

Table 3.3: Validation of inter-dataset-and-intra-subject universality. The validation was performed with ONH datasets. VOC denotes variance of the contributions and nISPV denotes normalized-ISPV. optimal indicates that the weights were optimized and w/o optimization indicates that the weights were not optimized but unities.

	Training-1 Subject-1	Test-1 Subject-1	Training-2 Subject-2	Test-2 Subject-2	Training-3 Subject-3	Test-3 Subject-3
VOC	0.000111	0.00244	0.0000304	0.00609	0.0000787	0.00446
Largest nISPV, optimal	0.551	0.592	0.567	0.590	0.541	0.586
Largest nISPV, w/o optimization	0.684	0.750	0.731	0.777	0.795	0.781

Table 3.4: Validation of inter-dataset-and-intra-subject universality. The validation was performed with macular datasets. VOC denotes variance of the contributions and nISPV denotes normalized-ISPV. optimal indicates that the weights were optimized and w/o optimization indicates that the weights were not optimized but unities.

	Training-1 Subject-2	Test-1 Subject-2	Training-2 Subject-4	Test-2 Subject-4	Training-3 Subject-1	Test-3 Subject-1
VOC	0.000111	0.00541	0.00000604	0.00307	0.00000785	0.00944
Largest nISPV, optimal	0.553	0.604	0.552	0.582	0.546	0.609
Largest nISPV, w/o optimization	0.648	0.676	0.641	0.656	0.630	0.627

in the choroid.

Training in Table 3.5 and Table 3.6 were the same as the Training in Table 3.1 and Table 3.2, respectively.

To summarize, a specific set of optimal weights was applicable among the B-scans in the same measurement dataset. However, it was not always applicable to other datasets and other subjects.

3.5.3 Computational time

The computational time of superpixel generation was dominated by three aspects: 6-D distance calculation, centroid calculation, and connectivity enforcement process.

The distance calculation measures the distance between the centroids from each superpixel to each image pixels. The distance calculation was performed approximately

Table 3.5: Validation of inter-subject universality. The validation was performed with ONH datasets. VOC denotes the variance of the contributions and nISPV denotes the normalized-ISPV. optimal indicates that the weights were optimized and w/o optimization indicates that the weights were not optimized but unities.

	Training Subject-1	Test-1 Subject-3	Test-2 Subject-4	Test-3 Subject-2
VOC	0.000111	0.00368	0.00373	0.00516
Largest nISPV, optimal	0.551	0.603	0.571	0.587
Largest nISPV, w/o optimization	0.684	0.731	0.795	0.746

Table 3.6: Validation of inter-subject universality. The validation was performed with macular datasets. VOC denotes the variance of contributions and nISPV denotes the normalized-ISPV. optimal indicates that the weights were optimized and w/o optimization indicates that the weights were not optimized but unities.

	Training Subject-2	Test-1 Subject-3	Test-2 Subject-4	Test-3 Subject-1
VOC	0.0000700	0.0116	0.0165	0.00602
Largest nISPV, optimal	0.553	0.627	0.614	0.567
Largest nISPV, w/o optimization	0.648	0.731	0.641	0.630

$4N$ -times, where N is the number of image pixels. The factor of four was selected because the distance computation was performed only for the image pixels, which was in an area with a size of $2S \times 2S$ centered at the centroid, where S is the interval among the initial superpixels. Thus, the distance was computed approximately four times on average for each image pixel. According to Eqs. (3.1)–(3.3), the computational time for a single distance calculation is approximately estimated as

$$\begin{aligned}
 \tau_D &= [(\tau_a + 2\tau_m)n_o + (n_o - 1)\tau_a + \tau_{sqr}] + [(\tau_a + \tau_m)n_s + (n_s - 1)\tau_a + \tau_{sqr}] \\
 &= 2(n_o + n_s - 1)\tau_a + (2n_o + n_s)\tau_m + 2\tau_{sqr},
 \end{aligned} \tag{3.10}$$

where τ_m , τ_a , and τ_{sqr} are the computational times for single multiplication, single addition, and square root operations, respectively. n_o and n_s are the numbers of optical features and spatial dimensions, respectively. The first and second pairs of square brackets in the first line represent the computational times of Eqs. (3.1) and (3.2), respectively. The first terms of each part correspond to the computational time for each operation in the summation (\sum), and the second terms represent the summation itself. The computational time for the total distance calculation is estimated to be $4N\tau_D$.

The total computational time for the centroid τ_C is estimated to be

$$\begin{aligned}
 \tau_C &= (n_o + n_s) \left[\sum_{k=0}^{K-1} (N_k - 1)\tau_a + K\tau_d \right] \\
 &= (n_o + n_s) [(N - K)\tau_a + K\tau_m],
 \end{aligned} \tag{3.11}$$

where N_k is the number of image pixels in the k -th superpixel and τ_d is the unit computational time for a single division. To derive the second line, I assumed that the unit computational times for single division and single multiplication were the same, that is, $\tau_d = \tau_m$.

The computational time for connectivity enforcement is highly dependent on its algorithm. Thus, I consider it as a black box, and denote it as τ_{CE} .

The total computational time for superpixel generation is approximately estimated as

$$\tau_{total} \simeq [4N\tau_D + \tau_C] \iota + \tau_{CE}, \quad (3.12)$$

where ι is the number of iterations in the superpixel reshaping process. Although ι nonlinearly varies by the compactness factor, it can be regarded as a constant for the realistic values of the compactness factor. By substituting Eqs. (3.10) and (3.11) into Eq. (3.12), and assuming τ_a is negligibly small and $\tau_a \ll \tau_m$, Eq. (3.12) becomes

$$\tau_{total} \sim \{[(8n_o + 4n_s)\tau_m + 8\tau_{sqr}]N + (n_o + n_s)\tau_m K\} \iota + \tau_{CE}. \quad (3.13)$$

By assuming $\tau_{sqr} \simeq \tau_m$ and substituting the parameters of this particular study, $n_o = 4$ and $n_s = 2$ into Eq. (3.13), the total computational time is approximately, but finally, estimated as

$$\tau_{total} \sim \iota(48N + 6K)\tau_m + \tau_{CE}. \quad (3.14)$$

This approximate estimation suggests that the number of image pixels (N) has approximately an eight times higher impact on the computational time than the number of superpixels (K) by omitting τ_{CE} .

As approximately, but theoretically, estimated above, the computational time of the superpixel generation algorithm varies by the number of superpixels, compactness factor, and particular algorithm implementation. In this study, the number of superpixels was 6,533 and the compactness factor was five. In this implementation, the core part of superpixel generation, which was indicated in the dashed and dotted blue square in the optimization chart (Fig. 3.1), took approximately 65 s for a B-scan. The weight optimizing process, including superpixel generation (dashed green box in Fig. 3.1) took approximately 22 min. Because weight optimization includes the superpixel generation process, the entire optimization (solid red box) took 22 min $\times n_i$, where n_i is the number of iterations required to determine the optimal compactness factor. The computation was performed using an Intel Core i7 4219HQ CPU with a clock frequency of 2.3 GHz.

3.6 Conclusions

I developed a new superpixel method specially tailored to multifunctional JM-OCT. A systemic optimization method for parameters in the superpixel algorithm was presented. The performance of the optimization method was evaluated in detail and it was found to work correctly. The superpixel method was applied to retinal OCT, and the generated superpixels were found to well preserve the tissue structures. Hence, the superpixel is expected to be a more suitable kernel for local statistics computation than the conventional uniform rectangular kernel. Local statistics with the superpixel kernel may enable more accurate quantitative analysis.

I developed an accurate birefringence measurement method based on superpixels which use spatial proximity and similarity of optical features obtained by JM-OCT. The larger Bhattacharyya distance suggests that the MAP birefringence estimation with the

superpixel kernel has better tissue discrimination ability. It may be because of its better quantification power of tissue birefringence.

Chapter 4

Conclusions

I developed an algorithm for differentiating between tissues in anterior eye on the basis of their optical properties provided by PS-OCT (the same information of the optical properties can be obtained by multifunctional JM-OCT). Five tissue types: conjunctiva, sclera, TM, cornea, and uvea were well separated in the 3D feature space and they were successfully discriminated.

I also developed the generation method of superpixels as image processing kernels for Multifunctional JM-OCT. BR estimated with superpixel kernels improved discrimination ability of the NFL in posterior eye.

Hence, I can conclude that multifunctional JM-OCT has a great advantage for tissue discrimination in anterior and posterior eye.

References

- [1] M. R. Hee, D. Huang, E. A. Swanson, and J. G. Fujimoto, “Polarization-sensitive low-coherence reflectometer for birefringence characterization and ranging,” *JOSA B* **9**, 903–908 (1992).
- [2] J. F. de Boer, T. E. Milner, M. J. C. van Gemert, and J. S. Nelson, “Two-dimensional birefringence imaging in biological tissue by polarization-sensitive optical coherence tomography,” *Optics Letters* **22**, 934–936 (1997).
- [3] E. Götzinger, M. Pircher, W. Geitzenauer, C. Ahlers, B. Baumann, S. Michels, U. Schmidt-Erfurth, and C. K. Hitzenberger, “Retinal pigment epithelium segmentation by polarization sensitive optical coherence tomography,” *Opt. Express* **16**, 16410–16422 (2008).
- [4] S. Makita, Y.-J. Hong, M. Miura, and Y. Yasuno, “Degree of polarization uniformity with high noise immunity using polarization-sensitive optical coherence tomography,” *Opt. Lett.* **39**, 6783–6786 (2014).
- [5] B. Baumann, S. O. Baumann, T. Konegger, M. Pircher, E. Götzinger, F. Schlanitz, C. Schütze, H. Sattmann, M. Litschauer, U. Schmidt-Erfurth, and C. K. Hitzenberger, “Polarization sensitive optical coherence tomography of melanin provides intrinsic contrast based on depolarization,” *Biomed. Opt. Express* **3**, 1670–1683 (2012).
- [6] Y. Jia, O. Tan, J. Tokayer, B. Potsaid, Y. Wang, J. J. Liu, M. F. Kraus, H. Subhash, J. G. Fujimoto, J. Hornegger, and D. Huang, “Split-spectrum amplitude-decorrelation angiography with optical coherence tomography,” *Opt. Express* **20**, 4710–4725 (2012).
- [7] S. Makita, K. Kurokawa, Y.-J. Hong, M. Miura, and Y. Yasuno, “Noise-immune complex correlation for optical coherence angiography based on standard and Jones matrix optical coherence tomography,” *Biomed. Opt. Express* **7**, 1525–1548 (2016).
- [8] Y. Lim, Y.-J. Hong, L. Duan, M. Yamanari, and Y. Yasuno, “Passive component based multifunctional Jones matrix swept source optical coherence tomography for Doppler and polarization imaging,” *Opt. Lett.* **37**, 1958–1960 (2012).
- [9] M. J. Ju, Y.-J. Hong, S. Makita, Y. Lim, K. Kurokawa, L. Duan, M. Miura, S. Tang, and Y. Yasuno, “Advanced multi-contrast Jones matrix optical coherence tomography for Doppler and polarization sensitive imaging,” *Opt. Express* **21**, 19412–19436 (2013).

- [10] D. Huang, E. A. Swanson, C. P. Lin, J. S. Schuman, W. G. Stinson, W. Chang, M. R. Hee, T. Flotte, K. Gregory, C. A. Puliafito, and J. G. Fujimoto, "Optical coherence tomography," *Science* **254**, 1178–1181 (1991).
- [11] H. Ishikawa, D. M. Stein, G. Wollstein, S. Beaton, J. G. Fujimoto, and J. S. Schuman, "Macular Segmentation with Optical Coherence Tomography," *Investigative ophthalmology & visual science* **46**, 2012–2017 (2005).
- [12] M. Mujat, R. Chan, B. Cense, B. Park, C. Joo, T. Akkin, T. Chen, and J. de Boer, "Retinal nerve fiber layer thickness map determined from optical coherence tomography images," *Optics Express* **13**, 9480–9491 (2005).
- [13] S. Asrani, M. Sarunic, C. Santiago, and J. Izatt, "Detailed Visualization of the Anterior Segment Using Fourier-Domain Optical Coherence Tomography," *Archives of ophthalmology* **126**, 765–771 (2008).
- [14] C. Xu, J. M. Schmitt, S. G. Carlier, and R. Virmani, "Characterization of atherosclerosis plaques by measuring both backscattering and attenuation coefficients in optical coherence tomography," *Journal of Biomedical Optics* **13**, 034003 (2008).
- [15] M. Pircher, E. Götzinger, R. Leitgeb, and C. K. Hitzenberger, "Transversal phase resolved polarization sensitive optical coherence tomography," *Physics in Medicine and Biology* **49**, 1257–1263 (2004).
- [16] M. Yamanari, S. Makita, and Y. Yasuno, "Polarization-sensitive swept-source optical coherence tomography with continuous source polarization modulation," *Optics Express* **16**, 5892–5906 (2008).
- [17] T. Gambichler, G. Moussa, M. Sand, D. Sand, P. Altmeyer, and K. Hoffmann, "Applications of optical coherence tomography in dermatology," *J. Dermatol. Sci.* **40**, 85–94 (2005).
- [18] S. A. Boppart, B. E. Bouma, C. Pitris, G. J. Tearney, J. F. Southern, M. E. Brezinski, and J. G. Fujimoto, "Intraoperative assessment of microsurgery with three-dimensional optical coherence tomography." *Radiology* **208**, 81–86 (1998).
- [19] V. Westphal, A. M. Rollins, J. Willis, M. V. Sivak, and J. A. Izatt, "Correlation of endoscopic optical coherence tomography with histology in the lower-GI tract," *Gastrointestinal Endoscopy* **61**, 537–546 (2005).
- [20] A. M. Sergeev, V. M. Gelikonov, G. V. Gelikonov, F. I. Feldchtein, R. V. Kuranov, N. D. Gladkova, N. M. Shakhova, L. B. Snopova, A. V. Shakhov, I. A. Kuznetzova, A. N. Denisenko, V. V. Pochinko, Y. P. Chumakov, and O. S. Streltzova, "In vivo endoscopic OCT imaging of precancer and cancer states of human mucosa," *Optics Express* **1**, 432–440 (1997).
- [21] A. V. DAmico, M. Weinstein, X. Li, J. P. Richie, and J. G. Fujimoto, "Optical coherence tomography as a method for identifying benign and malignant microscopic structures in the prostate gland - ScienceDirect," (2000).
- [22] K. W. Gossage, T. S. Tkaczyk, J. J. Rodriguez, and J. K. Barton, "Texture analysis of optical coherence tomography images: feasibility for tissue classification," *Journal of Biomedical Optics* **8**, 570–575 (2003).

- [23] X. Qi, M. V. Sivak, G. Isenberg, J. E. Willis, and A. M. Rollins, “Computer-aided diagnosis of dysplasia in Barrett’s esophagus using endoscopic optical coherence tomography,” *Journal of Biomedical Optics* **11**, 044010 (2006).
- [24] C. A. Lingley-Papadopoulos, M. H. Loew, M. J. Manyak, and J. M. Zara, “Computer recognition of cancer in the urinary bladder using optical coherence tomography and texture analysis,” *Journal of Biomedical Optics* **13**, 024003 (2008).
- [25] A. M. Zysk and S. A. Boppart, “Computational methods for analysis of human breast tumor tissue in optical coherence tomography images,” *Journal of Biomedical Optics* **11**, 054015 (2006).
- [26] D. C. Fernandez, H. M. Salinas, and C. A. Puliafito, “Automated detection of retinal layer structures on optical coherence tomography images,” *Optics Express* **13**, 10200–10216 (2005).
- [27] M. Szkulmowski, M. Wojtkowski, B. Sikorski, T. Bajraszewski, V. J. Srinivasan, A. Szkulmowska, J. J. Kaluzny, J. G. Fujimoto, and A. Kowalczyk, “Analysis of posterior retinal layers in spectral optical coherence tomography images of the normal retina and retinal pathologies,” *Journal of Biomedical Optics* **12**, 041207 (2007).
- [28] Y. Yasuno, V. D. Madjarova, S. Makita, M. Akiba, A. Morosawa, C. Chong, T. Sakai, K.-P. Chan, M. Itoh, and T. Yatagai, “Three-dimensional and high-speed swept-source optical coherence tomography for in vivo investigation of human anterior eye segments,” *Opt. Express* **13**, 10652–10664 (2005).
- [29] L. M. Sakata, R. Lavanya, D. S. Friedman, H. T. Aung, S. K. Seah, P. J. Foster, and T. Aung, “Assessment of the scleral spur in anterior segment optical coherence tomography images,” *Archives of Ophthalmology (Chicago, Ill.: 1960)* **126**, 181–185 (2008).
- [30] Y. Yasuno, M. Yamanari, K. Kawana, T. Oshika, and M. Miura, “Investigation of post-glaucoma-surgery structures by three-dimensional and polarization sensitive anterior eye segment optical coherence tomography,” *Optics Express* **17**, 3980–3996 (2009).
- [31] K. Kawana, T. Kiuchi, Y. Yasuno, and T. Oshika, “Evaluation of trabeculectomy blebs using 3-dimensional cornea and anterior segment optical coherence tomography,” *Ophthalmology* **116**, 848–855 (2009).
- [32] R. Duda, P. Hart, and D. Stork, “Pattern classification, 2nd ed,” Wiley, New York (2001).
- [33] M. Mujat, R. D. Ferguson, D. X. Hammer, C. Gittins, and N. Iftimia, “Automated algorithm for breast tissue differentiation in optical coherence tomography,” *Journal of Biomedical Optics* **14**, 034040 (2009).
- [34] C. Hitzenberger, E. Göetzing, M. Sticker, M. Pircher, and A. Fercher, “Measurement and imaging of birefringence and optic axis orientation by phase resolved polarization sensitive optical coherence tomography,” *Optics Express* **9**, 780–790 (2001).

- [35] B. H. Park, M. C. Pierce, B. Cense, and J. F. de Boer, “Jones matrix analysis for a polarization-sensitive optical coherence tomography system using fiber-optic components,” *Optics letters* **29**, 2512–2514 (2004).
- [36] M. Todorovi, S. Jiao, L. V. Wang, and G. Stoica, “Determination of local polarization properties of biological samples in the presence of diattenuation by use of Mueller optical coherence tomography,” *Optics Letters* **29**, 2402–2404 (2004).
- [37] N. J. Kemp, H. N. Zaatari, J. Park, H. G. R. Iii, and T. E. Milner, “Form-biattenuance in fibrous tissues measured with polarization-sensitive optical coherence tomography (PS-OCT),” *Optics Express* **13**, 4611–4628 (2005).
- [38] B. H. Park, C. Saxer, S. M. Srinivas, J. S. Nelson, and J. F. de Boer, “In vivo burn depth determination by high-speed fiber-based polarization sensitive optical coherence tomography,” *Journal of Biomedical Optics* **6**, 474–479 (2001).
- [39] B. Cense, T. C. Chen, B. H. Park, M. C. Pierce, and J. F. de Boer, “Thickness and birefringence of healthy retinal nerve fiber layer tissue measured with polarization-sensitive optical coherence tomography,” *Investigative Ophthalmology & Visual Science* **45**, 2606–2612 (2004).
- [40] S. Makita, M. Yamanari, and Y. Yasuno, “In vivo depth-resolved tissue contrast by local birefringence and differential optic axis orientation using polarization-sensitive swept-source optical coherence tomography,” (*International Society for Optics and Photonics*, 2009), vol. 7168, p. 71682H.
- [41] M. Yamanari, S. Makita, V. D. Madjarova, T. Yatagai, and Y. Yasuno, “Fiber-based polarization-sensitive Fourier domain optical coherence tomography using B-scan-oriented polarization modulation method,” *Optics Express* **14**, 6502–6515 (2006).
- [42] M. Yamanari, Y. Lim, S. Makita, and Y. Yasuno, “Visualization of phase retardation of deep posterior eye by polarization-sensitive swept-source optical coherence tomography with 1-m probe,” *Optics Express* **17**, 12385–12396 (2009).
- [43] M. Yamanari, M. Miura, S. Makita, T. Yatagai, and Y. Yasuno, “Phase retardation measurement of retinal nerve fiber layer by polarization-sensitive spectral-domain optical coherence tomography and scanning laser polarimetry,” *Journal of Biomedical Optics* **13**, 014013 (2008).
- [44] E. A. Swanson and J. G. Fujimoto, “The ecosystem that powered the translation of OCT from fundamental research to clinical and commercial impact [Invited],” *Biomed. Opt. Express* **8**, 1638–1664 (2017).
- [45] C. A. Puliafito, M. R. Hee, C. P. Lin, E. Reichel, J. S. Schuman, J. S. Duker, J. A. Izatt, E. A. Swanson, and J. G. Fujimoto, “Imaging of macular diseases with optical coherence tomography,” *Ophthalmology* **102**, 217–229 (1995).
- [46] M. Pircher, C. K. Hitzenberger, and U. Schmidt-Erfurth, “Polarization sensitive optical coherence tomography in the human eye,” *Prog. Retin. Eye Res.* **30**, 431–451 (2011).

- [47] J. F. d. Boer, C. K. Hitzenberger, and Y. Yasuno, “Polarization sensitive optical coherence tomography – a review [Invited],” *Biomed. Opt. Express* **8**, 1838–1873 (2017).
- [48] S. Guo, J. Zhang, L. Wang, J. S. Nelson, and Z. Chen, “Depth-resolved birefringence and differential optical axis orientation measurements with fiber-based polarization-sensitive optical coherence tomography,” *Opt. Lett.* **29**, 2025–2027 (2004).
- [49] S. Makita, M. Yamanari, and Y. Yasuno, “Generalized Jones matrix optical coherence tomography: performance and local birefringence imaging,” *Opt. Express* **18**, 854–876 (2010).
- [50] D. Kasaragod, S. Makita, S. Fukuda, S. Beheregaray, T. Oshika, and Y. Yasuno, “Bayesian maximum likelihood estimator of phase retardation for quantitative polarization-sensitive optical coherence tomography,” *Opt. Express* **22**, 16472–16492 (2014).
- [51] M. Yamanari, S. Tsuda, T. Kokubun, Y. Shiga, K. Omodaka, Y. Yokoyama, N. Himori, M. Ryu, S. Kunitatsu-Sanuki, H. Takahashi, K. Maruyama, H. Kunikata, and T. Nakazawa, “Fiber-based polarization-sensitive OCT for birefringence imaging of the anterior eye segment,” *Biomed. Opt. Express* **6**, 369–389 (2015).
- [52] S. Sugiyama, Y.-J. Hong, D. Kasaragod, S. Makita, S. Uematsu, Y. Ikuno, M. Miura, and Y. Yasuno, “Birefringence imaging of posterior eye by multi-functional Jones matrix optical coherence tomography,” *Biomed. Opt. Express* **6**, 4951–4974 (2015).
- [53] W. C. Y. Lo, M. Villiger, A. Golberg, G. F. Broelsch, S. Khan, C. G. Lian, W. G. Austen, M. Yarmush, and B. E. Bouma, “Longitudinal, 3d Imaging of Collagen Remodeling in Murine Hypertrophic Scars *In Vivo* using Polarization-sensitive Optical Frequency Domain Imaging,” *J. Invest. Dermatol.* **136**, 84–92 (2016).
- [54] E. Li, S. Makita, Y.-J. Hong, D. Kasaragod, and Y. Yasuno, “Three-dimensional multi-contrast imaging of in vivo human skin by Jones matrix optical coherence tomography,” *Biomed. Opt. Express* **8**, 1290–1305 (2017).
- [55] D. Kasaragod, S. Makita, Y.-J. Hong, and Y. Yasuno, “Noise stochastic corrected maximum a posteriori estimator for birefringence imaging using polarization-sensitive optical coherence tomography,” *Biomed. Opt. Express* **8**, 653–669 (2017).
- [56] C. Ahlers, E. Götzinger, M. Pircher, I. Golbaz, F. Prager, C. Schütze, B. Baumann, C. K. Hitzenberger, and U. Schmidt-Erfurth, “Imaging of the retinal pigment epithelium in age-related macular degeneration using polarization-sensitive optical coherence tomography,” *Invest. Ophthalmol. Vis. Sci.* **51**, 2149–2157 (2010).
- [57] B. Baumann, S. Zotter, M. Pircher, E. Götzinger, S. Rauscher, M. Glösmann, J. Lammer, U. Schmidt-Erfurth, M. Gröger, and C. K. Hitzenberger, “Spectral degree of polarization uniformity for polarization-sensitive OCT,” *J. Mod. Opt.* **62**, 1758–1763 (2015).
- [58] S. Makita, Y. Hong, M. Yamanari, T. Yatagai, and Y. Yasuno, “Optical coherence angiography,” *Opt. Express* **14**, 7821–7840 (2006).

- [59] L. An and R. K. Wang, “In vivo volumetric imaging of vascular perfusion within human retina and choroids with optical micro-angiography,” *Opt. Express* **16**, 11438–11452 (2008).
- [60] S. Kwon, Y. Yoon, B. Kim, W. H. Jang, B. Oh, K. Y. Chung, and K. H. Kim, “Dermoscopy guided dark-field multi-functional optical coherence tomography,” *Biomed. Opt. Express* **8**, 1372–1381 (2017).
- [61] X. Ren and J. Malik, “Learning a classification model for segmentation,” *Proc. Ninth IEEE Int. Conf. Comp. Vis.* pp. 10–17 vol.1 (2003).
- [62] R. Achanta, A. Shaji, K. Smith, A. Lucchi, P. Fua, and S. Süssstrunk, “SLIC Superpixels,” EPFL Technical Report 149300 (2010).
- [63] R. Achanta, A. Shaji, K. Smith, A. Lucchi, P. Fua, and S. Süssstrunk, “SLIC Superpixels Compared to State-of-the-Art Superpixel Methods,” *IEEE Trans. Pattern Anal. Mach. Intell.* **34**, 2274–2282 (2012).
- [64] American National Standard Institute, *American National Standard for the Safe Use of Lasers ANSI Z 136.1-2014* (American National Standards Institute, New York, 2014).